ENGINEERING PHYSICS FINAL DEGREE THESIS

PEI based selective contact for different photovoltaic absorber materials

Author
David ROVIRA FERRER

Supervisors
Dr. Joaquim PUIGDOLLERS
Dr. Edgardo SAUCEDO

Barcelona,
June 2021

Abstract

Research in photovoltaic (PV) devices has usually focused on PN junction theory. However, with the new perspective on electronic transport driven by eloctrochemical potentials rather than electrical fields, the understanding of solar cells as the combination of an absorber and two selective contacts has gained strength. As a consequence, there has been a growing interest in researching new selective contacts to obtain high efficiency and low-temperature processed photovoltaic devices that can reduce their cost and ecological footprint.
In this work, we report the promising performance obtained with a "Metal-Dipolar-Semiconductor" junction based on Polyethylenimine (PEI) as electron transport layer. Electrical and optical characterization have been performed to determine the contact quality over different absorbers, and a theoretical model explaining these results has been presented. Different photovoltaic devices have been fabricated and characterized, finding promising free-dopant and CRM-free architectures for different absorbers.
Currently, the global photovoltaic market is dominated by crystalline silicon (c-Si) based technologies with heavily doped, directly metallized contacts, which implies high-temperature steps. With the simple deposition of PEI between the semiconductor and the metal through spin-coating technique, we were able to obtain high-performance contacts without doping. In addition, regarding the study over thin-film absorbers, where the use of critical raw materials (CRM) is one of their main drawbacks, we proved that a stack combining a zinc oxide buffer layer and the polymeric interlayer yields outputs comparable to the classical CdS selective contact.

Acknowledgements

I would first like to thank Eloi Ros Costals, PhD student in the Department of Electronics, who has mentored me in my first steps in the photovoltaic research field and whose expertise was invaluable in formulating the methodology. Your insightful feedback brought my work to a higher level.

I would like to acknowledge my project directors, Dr. Joaquim Puigdollers and Dr. Edgardo Saucedo, for affording me the possibility to collaborate with their group and for their valuable advices and guidance along all the project duration.

I would also like to thank Dr. Cristoval Voz and Dr. Pablo Rafael Ortega, for opening me their place of work and for successfully answering and discussing my questions and results, which were very helpful for the advances in the project.

In addition, I would like to thank MNT and clean room team for assisting me in all moment. Specially grateful to Gema and Miguel (clean room staff) and to Benjamin, Estefania and Thomas (PhD students).

Finally, I also acknowledge the researchers at CUSTOM-ART and SENSATE projects, specially to Maykel and Alex Jiménez, for providing me samples and information of antimony selenide and kesterite absorbers.

Figure 1: Clean room group photo. From left to right: Thomas Tom (PhD student at UB), Gema Lopez (Lab technician and UPC professor), Isaac Montsech (master student), Alex Jiménez (PhD studen at CUSTOM-ART project), Eloi Ros (PhD student at UPC) and me, David Rovira.

Contents

Chapter 1

Introduction

Since the early stages of the industrial revolution and of global trade, society has been based on a continuous cycle of production and consumption, where the accumulation of goods and market expansion have been considered as "progress". This system has resulted in great benefits for the general community, such as a 40 year increase in life expectancy [1], the emergence of the welfare state and a remarkable technological and scientific development. However, due to its fast pace, only sustainable with a relentless energy supply, a growing number of drawbacks have emerged: regional borders and limits have been blurred, problems have become global, and, critically, environmental and climate degradation threaten life, as we know.

In recent years these problems have sparked the signing of a growing number of international initiatives and agreements, among which we can highlight the Paris Agreement on Climate Change or the European Green Deal, with the decarbonization of the economy, ecological footprint reduction and the need to limit global warming to +1.5ºC with respect to pre-industral temperatures as their main purposes. It is clear, thus, that a change must be made both in the economic model and in power generation. The project presented here is set as a part of the latter mentioned change.

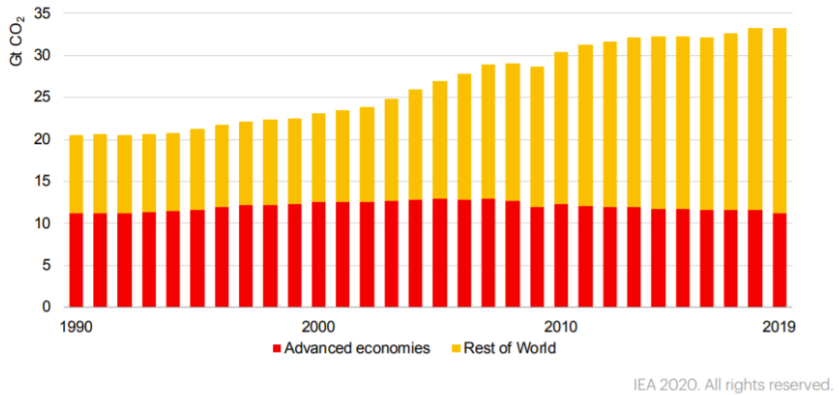

Figure 1.1: Energy-related CO2 emissions, 1990-2019. [2]

Nowadays, fossil fuel based energy sources are the predominant ones in the global energy economy, with practically 80% of the share in total primary energy demand [2]. Although in the previous years we have seen efficiency improvements in the energy conversion to electricity and a growth in renewable energy installations, CO_2 emissions continue to trend upward. It is clear that proper investments in renewable energy facilities must be addressed in the coming years if carbon neutrality is to be achieved

by 2050. There are many renewable energy alternatives, with photovoltaic generation appearing to have the greatest potential, as hydroelectric and wind power generation are limited by their biosphere impact and topographic limitations. Even then, if photovoltaic generation is to fulfill its potential, some aspects have to be addressed, such as a shift in the energy peak demand to maximum production hours in order to reduce the impact of energy storage issues [3, 4].

However, as the most common solar cell architecture on the market is based on silicon absorber and the use of an entire rear surface alloyed with aluminium [5, 6], the energy return on investment is reduced. This is because, in order to obtain a good contact between the electrode and the silicon, the interface must be heavily doped, which is done by high temperature diffusion of phosphorous or boron ($\sim 1000^{\circ}C$). Thus, low temperature processes are desired in order to enhance metal-semiconductor junctions. The most extensive approach for this purpose is the use of silicon heterojunction (SHJ) solar cells, where selective contacts are deposited over the absorber instead of diffusing a dopant into it.

These "dopant-free" approaches can generally be included within Metal-Insulator- Semiconductor (MIS) contacts, where their main effect is to passivate semiconductor surface and block the transport of one type of carrier. They can involve from metal oxides to organic materials, passing through low-dimensional semiconductors. Unlike this last approach, where timid results have been obtained with efficiencies below 15% [7, 8]; the low temperature and versatility of deposition techniques, coupled with the wide range of materials offered by the other two approaches, make them a promising industrial alternative for doping contacts.

In particular, the use of small organic molecules or self-assembled monolayers has gained significant attention in recent years thanks to their simple and low-cost deposition techniques by dissolution, such as screen-printing or spin-coating. There are many examples, among which we can emphasize the well- known use of PEDOT:PSS as hole transmission layer (HTL), yielding efficiencies over 20% for full contacted area [9], and the use of PEI or PEIE layers as electron transmission layers (ETL) [10], where the charged or polar layers facilitate the transfer of carriers and their binding with superficial dangling bonds, thus reducing the barrier height at the interface.

Nevertheless, as the amount of silicon employed in these commercial devices is considerable and is susceptible to geopolitical tensions, research in thin-film absorbers made up of non-critical materials is considered, currently, a hot topic. In this sense, direct band gap semiconductors are sought due to their significant absorption of sunlight in thin layers of a few micrometers. The most prominent examples of these materials are amorphous silicon, kesterites and antimony sulphide, which do not involve critical raw materials. However, they still present important limitations such as degradation due to light exposure and undesired secondary phases that cause failures in PCE extraction above 15% [11, 12]. For this reason, the upcoming strategy present in this work to mitigate these limitations is to incorporate the organic heterojunction approach into these thin-film absorbers.

Chapter 2

Theoretical Background

2.1 What are semiconductors? Band theory

[13][14][15]

In order to know which kind of mathematical representation one should use for electrons inside a semiconductor material we have to modelize the setting in which the electron is found. As general, we will consider the semiconductor as a solid crystalline structure which traps our electrons inside its physical edges. Then, as the electrons are confined (inside a distance L if we are in the 1-dimensional case), one can represent them as plane waves with a wavenumber given by $k_m = \frac{2\pi m}{L}$, with $m = 0, \pm 1, ..., \pm\frac{N}{2}$ being N the number of ions in the lattice. Also, as the electrons will be under a periodic potential due to the crystalline disposition of the semiconductor ions, specifically under periodic well potentials, these waves must be periodic with the crystal.
If we impose that our potential must respect the crystal periodicity we find, as one should expect from crystallography, the reciprocal lattice notation:

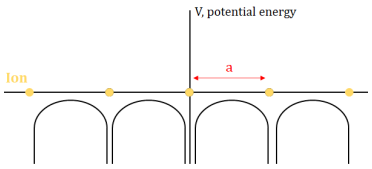

$$V(r) = V(r+a)$$

Figure 2.1: Potential profile of the crystal lattice and its periodicity condition.

where a is the crystal's lattice parameter. Then, one can write the potential in terms of a Fourier expansion:

$$V(r) = \sum_n V_n e^{ik_n r}, \text{ with } V_n \text{ being a well potential of length equal to ion's width, } b \tag{2.1a}$$

$$\sum_n V_n e^{ik_n r} = \sum_n V_n e^{ik_n (r+a)} \rightarrow k_n = \frac{2\pi n}{a} \equiv G_n \tag{2.1b}$$

which are exactly the 1D vectors of the reciprocal lattice. This result should not surprise the reader as the reciprocal lattice can be understood as the Fourier transform of the real space and, then, if we want a potential fulfilling the crystalline periodicity our Fourier basis must be the vectors of the crystal reciprocal lattice. With that, we can limit the study of the electron's Schrödinger solutions under this potential inside the first Brillouin Zone (unit cell) as the physical properties will be equivalent for the other zones.

If we expand to the 3D solid, the Fourier expansion for the potential will be given by the lattice vectors satisfying the condition $e^{i\vec{G}\cdot\vec{a}} = 1$:

$$V(\vec{r}) = \sum_G V_{\vec{G}} \cdot e^{i\vec{G}\cdot\vec{r}} = e^{i\vec{G}\cdot\vec{a}} \sum_G V_{\vec{G}} \cdot e^{i\vec{G}\cdot\vec{r}} = V(\vec{r}+\vec{a}) \tag{2.2}$$

Once we know the interaction field of the electrons with the lattice, we can find the wave function of one electron ($|\Psi(\vec{r})\rangle$) solving its corresponding Schrödinger equation:

$$\mathcal{H}\,|\Psi(\vec{r})\rangle = E\,|\Psi(\vec{r})\rangle \rightarrow [-\frac{\hbar^2}{2m}\nabla^2 + V(\vec{r})]\,|\Psi(\vec{r})\rangle = E\,|\Psi(\vec{r})\rangle \tag{2.3}$$

where $\mathcal{H}$ is the system's Hamiltonian with the periodic potential.
The most general hypothesis that one can assume as a solution of this equation, is to consider a wave function expansion of all the permitted plane waves:

$$|\Psi(\vec{r})\rangle = \sum_{\vec{k}} c_k e^{i\vec{k}\cdot\vec{r}} \tag{2.4}$$

Considering the periodic boundary conditions, the permitted $\vec{k}$ vectors must satisfy:

$$|\Psi(x,y,z)\rangle = |\Psi(x+L,y,z)\rangle = |\Psi(x,y+L,z)\rangle = |\Psi(x,y,z+L)\rangle \tag{2.5}$$

what ends to

$$k_x = \frac{2\pi n_x}{L};\; k_y = \frac{2\pi n_y}{L};\; k_z = \frac{2\pi n_z}{L} \tag{2.6}$$

with $n_{i=x,y,z}$ being integers. Finally, if we substitute both wave function and potential expressions into the Schrödinger equation, we obtain the next summatory equation:

$$\frac{\hbar^2}{2m}\sum_{\vec{k}} k^2\, c_k\, e^{i\vec{k}\cdot\vec{r}} + \sum_{\vec{k}}\sum_{\vec{G}} V_G\, c_k\, e^{i(\vec{k}+\vec{G})\cdot\vec{r}} = E\sum_{\vec{k}} c_k\, e^{i\vec{k}\cdot\vec{r}} \tag{2.7}$$

Then, as this equality must be satisfied for all value of $\vec{r}$ we can consider only one term of the $\vec{k}$ summatory (one plane wave, $\vec{k_i}$);

$$\frac{\hbar^2}{2m}\, k_i^2\, c_{k_i}\, e^{i\vec{k_i}\cdot\vec{r}} + \sum_{\vec{G}+\vec{k}=\vec{k_i}} V_G\, c_k\, e^{i(\vec{k}+\vec{G})\cdot\vec{r}} = E\, c_k\, e^{i\vec{k_i}\cdot\vec{r}} \tag{2.8a}$$

$$\frac{(\hbar k_i)^2}{2m} c_{k_i}\, e^{i\vec{k_i}\cdot\vec{r}} + \sum_{\vec{G}} V_G\, c_{\vec{k_i}-\vec{G}}\, e^{i\vec{k_i}\cdot\vec{r}} = E\, c_k\, e^{i\vec{k_i}\cdot\vec{r}} \tag{2.8b}$$

At the end we have obtained a set of linear equations that will give us the coefficients c_k and, then, the electron's wave function. Moreover, as only the coefficients differing a reciprocal lattice vector from the selected $\vec{k_i}$ are involved, one can simplify the coupled system by considering that $\vec{k_i}$ belongs to the first Brillouin zone (1BZ). Thus, as the summatory term will be shifts of the initial $\vec{k_i}$ to higher Brillouin zones which are equivalent (no vectors of the 1BZ will be found in the same equation) a decoupled system of N (number of atoms in the lattice) independent problems is obtained.
Thus, one can check that the wave function for the electron of wavenumber $\vec{k}$ will be the combination of its corresponding plane wave plus all the plane waves shifted by a reciprocal lattice vector:

$$|\Psi_k(\vec{r})\rangle = \sum_{\vec{G}} c_{\vec{k}-\vec{G}}\, e^{i(\vec{k}-\vec{G})\cdot\vec{r}} \tag{2.9}$$

which can be rearranged as:

$$|\Psi_k(\vec{r})\rangle = e^{i\vec{k}\cdot\vec{r}} \sum_{\vec{G}} c_{\vec{k}-\vec{G}}\, e^{-i\vec{G}\cdot\vec{r}} = U(\vec{r}) e^{i\vec{k}\cdot\vec{r}} \tag{2.10}$$

obtaining a Bloch wave, which is a plane wave (what ensures charge isotropy as the integration over all $\vec{k}-\vec{G}$ of these waves or charge/probability densities give a constant value) modulated by a funcion of $\vec{r}$ which respects the lattice periodicity; $U(\vec{r}) = U(\vec{r}+n\vec{a})$. Also, this solution is invariant under translations in the reciprocal space, maintaining the equivalence between different Brillouin zones, $E_{\vec{k}+\vec{G}} = E_{\vec{k}}$.
One of the most important results that one can extract from this Bloch's Theory is the appearance of energetic bands, i.e. regions of no possible states for the electrons (energy gaps). To understand how these bands arise, let's consider the simplest case of a quasifree electron, i.e. an infinitesimal potential $V = \delta V(\vec{r})$.
When $\delta = 0$, there is no potential and we have a free electron, without periodicity, whose energetic state can be described by Sommerfeld Model: $E_k = \frac{1}{2m}(\hbar k)^2$. However, if we consider an infinitesimal perturbation, $\delta \neq 0$ but $\delta \to 0$, we will have periodic delta potentials along the lattice. Then, we can consider the repetition of the parabolic energy profile at each Brillouin zone (Figure 2.2).

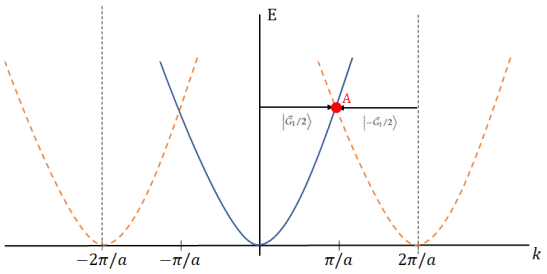

Figure 2.2: Dispersion curve for a free particle in empty lattice model.

But, if we do nothing, a degeneration problem will appear at each Brillouin boundary as the two adjacent Sommerfeld profiles cross, introducing an uncertainty with respect to which Brillouin zone the electron belongs. To solve this, let's study the solutions of the Schrödinger equation at the boundaries. As first appearence of energy levels depletion into bands, consider the degeneration found in the cross between the parabolas of the first and second Brillouin zones. The wave functions corresponding to this two energetic levels will be $|\Psi_{\vec{G}_1/2}(\vec{r})\rangle \equiv |\vec{G}_1/2\rangle$ and $|\Psi_{-\vec{G}_1/2}(\vec{r})\rangle \equiv |-\vec{G}_1/2\rangle$, where $\vec{G}_1$ is the first reciprocal lattice vector (for the 1D case would be $\frac{2\pi}{a}$). Probably, it will be clarifying to explicitly explain where the second wave function comes from. When one is studying the degenaration obtained due to the cross of two energetic profiles it has to write the states seen with respect to the coordinates of the Brillouin zone (BZ) which the profile belongs to. In our case, as it is the crossing between the parabolas of the first and second BZ at their border, the wave function corresponding at this point, seen from the 1BZ's origin is at a quasimomentum of $|\vec{G}_1/2\rangle$, while seen from the 2BZ's origin is at $|-\vec{G}_1/2\rangle$ (see point A of the figure above).
Once we have clear the states involved in the initial degeneration problem, we can study its depletion into bands by solving the Schrödinger equation. The system will be:

$$\begin{cases} \left|\vec{G}_1/2\right\rangle = c_{\frac{\vec{G}_1}{2}}\, e^{i\frac{\vec{G}_1\cdot\vec{r}}{2}} \\ \left|-\vec{G}_1/2\right\rangle = c_{-\frac{\vec{G}_1}{2}}\, e^{-i\frac{\vec{G}_1\cdot\vec{r}}{2}} \\ \left[\frac{(\hbar k_i)^2}{2m} - E\right]\cdot c_k + \sum_{\vec{G}} V_{\vec{G}} c_{\vec{k}_i-\vec{G}} = 0 \end{cases} \tag{2.11}$$

Let's analyse qualitatively the emergence of energy bands in order to have a more intuitive image of the band theory. The electron's wave function at the border of the 1BZ and 2BZ ($\vec{k} = \vec{k}_i$) will take the form of:

$$\left|\Psi_{\vec{k}_i}(\vec{r})\right\rangle = e^{i\vec{k}_i\cdot\vec{r}} \sum_{\vec{G}} c_{\vec{k}_i-\vec{G}} e^{-i\vec{G}\cdot\vec{r}} \tag{2.12}$$

where the coefficients are given by Schrödinger's equation:

$$c_{\vec{k}} = \frac{\sum_{\vec{G}} V_{\vec{G}} c_{\vec{k}_i-\vec{G}}}{\frac{(\hbar k_i)^2}{2m} - E} \tag{2.13}$$

where E will be the energy at each $\vec{k} = \vec{k}_i - \vec{G}$ given by the energy profile, initially the parabola one. Then, only those k's whose associated energy, E, are close to $\frac{(\hbar\vec{k}_i)^2}{2m}$ will have a significant contribution to the linear combination of $\left|\Psi_{k_i}(\vec{r})\right\rangle$. Only the $\vec{k} = \frac{\vec{G}_1}{2}$ and $\vec{k} = -\frac{\vec{G}_1}{2}$ will contribute to the wave function, while the rest of quasimomentums ($\pm\frac{\vec{G}1}{2} \pm n\frac{\vec{G}1}{2}$) would have E's too different from $\frac{(\hbar\vec{k}_i)^2}{2m}$ that their coefficients will be practically negligible, $c_k \to 0$. Then, the wave function at the this border can take two possible forms, the symmetric and the antisymmetric functions:

$$|\Psi_+(\vec{r})\rangle \approx e^{i\frac{\vec{G}_1\cdot\vec{r}}{2}} + e^{-i\frac{\vec{G}_1\cdot\vec{r}}{2}} \approx cos\left(\frac{\vec{G}_1}{2}\cdot\vec{r}\right) \tag{2.14a}$$

$$|\Psi_-(\vec{r})\rangle \approx e^{i\frac{\vec{G}_1\cdot\vec{r}}{2}} - e^{-i\frac{\vec{G}_1\cdot\vec{r}}{2}} \approx sin\left(\frac{\vec{G}_1}{2}\cdot\vec{r}\right) \tag{2.14b}$$

If we look now to the probability density given by these wave functions we see that they have the maximums and minimums exchanged:

$$Prob(|\Psi_+(\vec{r})\rangle) \propto cos^2\left(\frac{\vec{G}_1}{2}\cdot\vec{r}\right) \tag{2.15a}$$

$$Prob(|\Psi_+(\vec{r})\rangle) \propto sin^2\left(\frac{\vec{G}_1}{2}\cdot\vec{r}\right) \tag{2.15b}$$

The symmetric wave function has its maximum of probability at the minimum of the potential what will end into a decrease of the energy at the boarder with respect to the parabolic profile. In contrast, the antisymmetric wave function has its maximum at the maximum of the potential what will increase the energy of this state with respect to the parabolic one. Thus, we have a depletion of the parabolic profile into two bands (Figure 2.3a).

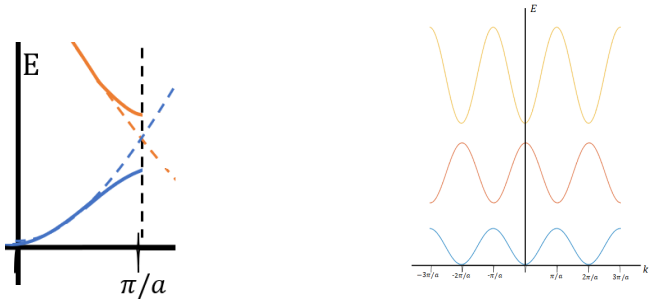

(a) (b)

Figure 2.3: (a) Gap appearence between the first and second Brillouin zones. (b) Energy bands for the nearly free electron model.

If we do a similar analysis for all the other degenerated points we will obtain the different energy bands (Figure 2.3b).
From these bands one can classify them into two types considering the occupancy level. If all the band is filled with electrons we talk about a valence band, while if the top band with electrons is not completely filled it is called a conduction band. Therefore, when a material has its last band completely filled, the crystal will be an insulator as the energy gap separating the electrons from the empty states prevent their movement (no electric current) when an electric field is applied (Figure 2.4b). In contrast, when a material has a band which is not completely filled, the electrons can acquire different momentum as there are available empty states, and, then, a current flows if we apply an electric field (Figure 2.4a). The material behaves as a metal.

(a) (b)

Figure 2.4: Comparison between a (a) non-full and, (b) full band behaviour under the application of an electric field.

In addition, we can make a distinction inside the insulators. When the band gap has an energy gap lower than $1.5eV$ the electrons can overpass it easily (only with thermal generation) and reach the conduction band in enough amount to give a non negligible current when an electric field is applied. These type of materials are called "semiconductors" and can be classified, at the same time, into two kinds: direct and indirect.

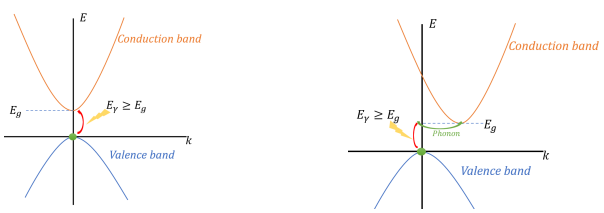

(a) (b)

Figure 2.5: Graphic representation of a direct (a) and indirect (b) semiconductors.

The direct ones are those semiconductors that has the minimum of the conduction band at the same momentum of the valence band maximum. These semiconductors

will only need an energy support to overpass the band gap, while the indirect semiconductors need the assistance of a phonon to supply the momentum difference present between the minimum of the conduction band and the maximum of the valence band. As the value of the density states will be of the order of the atoms concentration in the solid, i.e. $10^{23}cm^{-3}$, and the number of electrons that will have enough energy to jump the band gap and reach the conduction band will be much lower, around $10^{8}cm^{-3}$ [1], we can assume that these electrons will be around the conduction band minimum and then, the quasifree model can be considered for them. Thus, the energy profile can be approximated to $E(k) = E_c + \frac{(\hbar k)^2}{2m_e^*}$ for the conduction band and to $E(k) = E_v - \frac{(\hbar k)^2}{2m_h^*}$ for the valence band, being E_c the minimum energy in the conduction band and E_v the maximum energy in the valence band and the m_e^* and m_h^* the effective masses of an electron found respectively in the conduction and in the valence band. This effective mass is a tensor whose inverse describes the band curvature:

$$\frac{1}{m_{i,j}^*} = \frac{1}{\hbar^2}\frac{\partial^2 E(k)}{\partial k_i \delta k_j} \tag{2.16}$$

and for this 1D case simplifies to $m_e^* = \hbar^2(\frac{\partial^2 E(k)}{\partial^2 k})^{-1}$ and $m_h^* = -\hbar^2(\frac{\partial^2 E(k)}{\partial^2 k})^{-1}$.
Deeply, if we treat with a more realistic 3D solid we can have different bands depending on which crystalline direction the electron moves, as the potential interaction, i.e. the periodicity, can differ. Then, we can have multiple equivalent minimums for the conduction band but, by grouping terms, one can still use the approximated energy profile with a modified effective mass.
From this, one can know the carrier concentration (in thermal equilibrium), i.e. the charges that will contribute to the current generation. The carrier density in the conduction band will be given by the product of the density of available states in the conduction band and the probability of being occupied, i.e. the Fermi-Dirac distribution. For an electron in a 3D crystal of dimension L, the volume of one state in the reciprocal space will be $(2\pi/L)^3$, as for each crystalline direction we have that $k_i = n_i 2\pi/L$. Then, the number of states inside the shell $\vec{k}$ and $\vec{k} + d\vec{k}$ will be:

$$dN(\vec{k}) = g(k)d\vec{k} = \frac{2}{(2\pi/L)^3}d\vec{k} = 2\frac{4\pi k^2}{(2\pi/L)^3}dk \tag{2.17}$$

and writing it in terms of the energy instead of the quasimomentum:

$$E(k) = E_0 + \frac{(\hbar k)^2}{2m^*} \rightarrow k^2 = \frac{2m^*}{\hbar^2}\left(E(k) - E_0\right) \rightarrow dE = \frac{\hbar^2 k}{m^*}dk \rightarrow dk = \frac{m^*}{\hbar^2 k}dE \tag{2.18a}$$

$$dN(E) = 2\frac{4\pi k^2}{(2\pi/L)^3}\frac{m^*}{\hbar^2 k}dE = \frac{kL^3}{\pi^2}\frac{m^*}{\hbar^2}dE = \frac{L^3}{2\pi^2}\left(\frac{2m^*}{\hbar^2}\right)^{3/2}\sqrt{E - E_0}dE \tag{2.18b}$$

Finally, as the density of states, $D(E)$, is the number of states per unit of volume and energy, it will take the form of:

$$D(E) = \frac{1}{L^3}\frac{dN(E)}{dE} = \frac{1}{2\pi^2}4\pi\left(\frac{2m^*}{\hbar^2}\right)^{3/2}\sqrt{E - E_0} = 4\pi\left(\frac{2m^*}{h^2}\right)^{3/2}\sqrt{E - E_0} \tag{2.19}$$

[1] The number of electrons that can jump the band gap of a semiconductor ($Eg \sim 1.5eV$) will be given by the Fermi-Dirac formalism. From this we know that the probability of having an electron with energy E is $f(E) = [1 + e^{(E-E_f)/k_B T}]^{-1}$, where E_f is the Fermi level and represents the energy where the probability of having the state occupied is $1/2$. Then, taking $E = E_c$ in order to now the probability of an electron to reach the conduction band, we obtain that the density of electrons in this band is given by $n_c \sim 10^{23} \cdot f(E_c) \approx 10^{10}$, where we have taken a Fermi energy of an intrinsic semiconductor, approximately half the band gap.

Now, the concentration of electrons will be given by the product of this density of states when the energy is bigger than E_c and the probability of being occupied:

$$n = \int_{E_c}^{\infty} D_c(E) f(E) dE = \int_{E_c}^{\infty} 4\pi \left(\frac{2m^*}{h^2}\right)^{3/2} \sqrt{E - E_c} \left(1 + e^{(E-E_f)/k_B T}\right)^{-1} \tag{2.20}$$

and, if we consider a non-degenerate semiconductor where the number of carriers is much smaller than the density of states, i.e the probability of coinciding more than one carrier in the same state is practically null, the distinction between Fermi-Dirac and Boltzmann distributions tends to disappear. In other words, $E - E_f >> k_B T$ and then $f(E) \sim e^{-(E-E_f)/k_B T}$ simplifying the integration and leading to:

$$n \sim N_c \, e^{-(E_c - E_f)/k_B T}, \text{ with } N_c = 2 \left(\frac{2\pi m_e^* k_B T}{h^2}\right)^{3/2} \tag{2.21}$$

Acting in a similar way, but taking the probability of having the state unoccupied, one can obtain the concentration of holes:

$$p = \int_{-\infty}^{E_v} D_v(E)[1 - f(E)] dE = ... \sim N_v \, e^{-(E_f - E_v)/k_B T}, \text{ with } N_v = 2 \left(\frac{2\pi m_h^* k_B T}{h^2}\right)^{3/2} \tag{2.22}$$

If we do the product of both carrier concentration we find a constant value:

$$np = N_c N_v \, e^{-E_g/k_B T} = n_i^2 \tag{2.23}$$

being n_i the intrinsic carrier concentration. This equality is always satisfied if the semiconductor is not doped in excess, i.e. if it is a non-degenerate semiconductor. For a semiconductor without impurities and where all the electrons present in the conduction band come from the valence band receives the name of an *Intrinsic Semiconductor*. Then, for definition, the electron and hole concentration will be equal:

$$n = p \xrightarrow{np = n_i^2} E_f = E_i \tag{2.24}$$

And, its Fermi level is found practically in the middle of the band gap:

$$n = p \rightarrow N_c \, e^{-(E_c - E_i)/k_B T} = N_v \, e^{-(E_i - E_v)/k_B T} \rightarrow E_i = \frac{E_c + E_v}{2} - \frac{1}{2} k_B T \, ln \left(\frac{N_c}{N_v}\right) \tag{2.25}$$

On the contrary, if we have some impurities that supplies extra carriers, the Fermi level will be displaced. In this case we are talking of an *Extrinsic Semiconductor* and can be of two types:

- n-type: Here, we have donor impurities that dope with extra electrons the conduction band. Typically, these impurities are elements with a higher oxidation number that replace some crystal motif without being enough in number (N_d) to alter the crystallinity, but enough to contribute in the conduction. These extra electrons that are not shared in the crystal bonds will orbit around the cationic impurities with an energetic state very close to the conduction band, what will end to a low costly transfer of electrons to this band. Then, we have that the electron's density is much higher than the one corresponding to holes, $n >> n_i >> p$, and, therefore, the Fermi level is close to E_c.

- p-type: In contrast, the impurities (N_a) involved in these semiconductors can be defects in the lattice such as empty motifs or elements with a lower oxidation number. Then, we have that the remaining elements have to supply their electrons to maintain the structure, leaving holes in the valence band. Thus, the energetic level of these impurities must be close to the valence edge, in order to be easier to promote electrons to them instead of the conduction band.

To find the explicit carrier density for these extrinsic semiconductors, one has to solve the charge neutrality condition:

$$n + N_a^- = p + N_d^+ \tag{2.26}$$

knowing that $N_a^- = N_a f(E_A)$ and $N_d^+ = N_d[1 - f(Ed)]$. With this equation one can find both the carrier density and the Fermi level of the semiconductor at any temperature. At room temperature, $150K < T < 500K$, the thermal agitation is big enough to ionize all the donor impurities but not enough to promote significant electrons from the valence band to the conduction one. Then, one can assume that $n = N_d^+ = N_d$.

2.2 Carrier transport in semiconductors

The transport or movement of carriers inside semiconductor materials is mainly due two phenomena: movement as result of the concentration gradient of the same particles across the semiconductor (diffusion current) and as result of the force applied by an electric field (drift current). [16, 17, 18]

2.2.1 Diffusion current

When there is no electric field applying over our semiconductor, one can consider that the electrons of the conduction band moves with ideal gases kinetic:

$$\frac{3}{2}k_B T = \frac{1}{2}m_e^* v_{th}^2 = \frac{1}{2}m_e^*\left(v_x^2 + v_y^2 + v_z^2\right) = \frac{3}{2}m_e^* v_x^2 \tag{2.27a}$$

$$\langle v_x \rangle = \langle v_y \rangle = \langle v_z \rangle \tag{2.27b}$$

Then, considering the 1D case, the electrons move arbitrarily, so, they have the same probability of moving to the left and to the right. Thus, if we have a concentration gradient in the material, i.e. more electrons at the left, we will have an uncompensated flux of electrons from the left to the right and a current is observed (Figure 2.6).

Considering the transfer of electrons between regions with sizes of electron's mean free path, $l = v_x \tau_c$ where τ_c is the time between e^--atom collisions, one can obtain the current only drived by the concentration gradient. Considering the current passing through the sheet at x position, we have that half of the electrons found in the region $[x - l, x]$ will cross, in a time τ_c, our surface to the right neighbour region. And the same for the region $[x, x + l]$ but in the opposite direction. Thus, the final current density passing through our surface will be:

$$J_{n,diff} = -q\,\frac{\frac{1}{2}l\,n\left(x - \frac{l}{2}\right) - \frac{1}{2}l\,n\left(x + \frac{l}{2}\right)}{\tau_c} = \frac{1}{2}qlv_x\frac{dn}{dx} = \frac{1}{2}qv_x^2\tau_c\frac{dn}{dx} \tag{2.28}$$

and using the energy equipartition supposed in equation 2.27*a*:

$$J_{n,diff} = \frac{l}{2}\,\frac{q\,k_B T\,\tau_c}{m_e^*}\frac{dn}{dx} = q\,D_n\,\frac{dn}{dx} \tag{2.29}$$

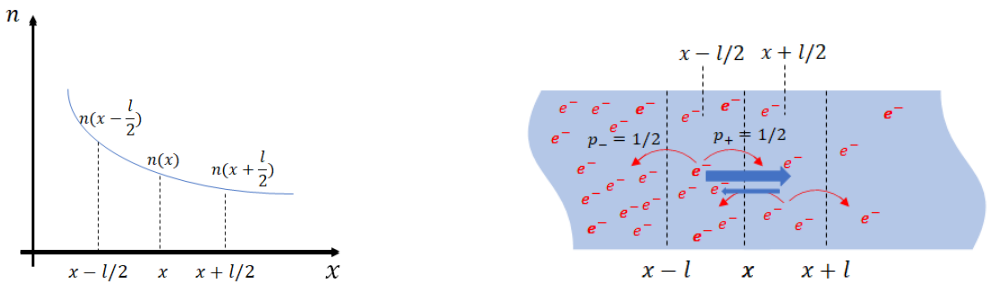

(a) (b)

Figure 2.6: (a) Plot of a non-homogeneous carrier concentration along semiconductors width and, (b) graphical representation of the current generation due to this non-homogeneity.

With that, and as one should have expected, the diffusion current is proportional to the concentration gradient by a factor D, called diffusivity. This is known as Fick's law:

$$J_{n,diff} = q\,D_n\,\frac{dn}{dx} \qquad \& \qquad J_{p,diff} = -q\,D_p\,\frac{dp}{dx} \tag{2.30}$$

2.2.2 Drift current

When an electric field is applied, the above aleatory movement gains a preferential direction in which the electron's mean velocity is non-null. The momentum gained by the electron ($p = v_e m_e^*$) during the electric field application will be proportional to this, $p \propto E$. This is because the momentum can be also defined through the classical mechanics impulse, $\vec{I} = \Delta\vec{p}$. With that, one can define the momentum as $\vec{p} = \vec{F}dt$, which in our case will take the form of $\vec{p} = -q\vec{E}\tau_c$, if we consider only the time between collisions.

$$\vec{v}_e = -\frac{q\tau_c}{m_e^*}\vec{E}, \qquad \text{between collisions.} \tag{2.31}$$

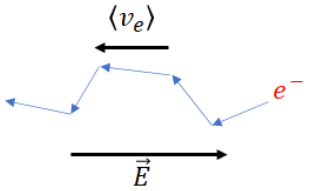

Figure 2.7: Representation of the non-null mean carrier velocity when an electric field is applied over the semiconductor.

But, as the electron will suffer, in average, a collision with the lattice motif, and then a complete loss of the velocity, at every τ_c period, the average velocity will be approximately half the above:

$$\vec{v}_{drift} = -\frac{1}{2}\frac{q\tau_c}{m_e^*}\vec{E} = -\mu_n\vec{E} \tag{2.32}$$

Then, the drift current density will be the sum of all electrons contribution, i.e. $J_n = I_n/A = \sum_i -qv_i$. Moreover, this total drift current can be substituted by the product of the mean drift velocity and the electron concentration: $-qnv_e = qn\mu_n E$. Thus, the total drift current, including both electron and hole drift currents, will be:

$$J_{drift} = \left[q\,n\,\mu_n + q\,p\,\mu_p\right]\,E = \sigma\,E \tag{2.33}$$

where σ is the conductivity of the material and it is the inverse of the resistivity. Finally, the total current will be the sum of both types:

$$J_n = q\,n\,\mu_n\,E + q\,D_n\,\frac{dn}{dx} \tag{2.34a}$$

$$J_p = q\,p\,\mu_p\,E - q\,D_p\,\frac{dp}{dx} \tag{2.34b}$$

In thermal equilibrium the current of both carriers will be zero as the carrier concentration must remain constant. Thus, the diffusion and drift current contrarest one to each other and knowing that the electron concentration is $n = n_i\,e^{(E_c - E_i)/k_B T}$ one can conclude that in equilibrium the Fermi level remains constant:

$$J_n = 0 = q\,n\,\mu_n\,E + q\,D_n\,\frac{dn}{dx} \xrightarrow{n = n_i\,e^{(E_c - E_i)/k_B T}} J_n = \mu_n\,n\,\frac{dE_f}{dx} = 0 \tag{2.35}$$

In summary, under equilibrium state the semiconductor is fully characterized by a constant Fermi level which gives us the carriers density and makes zero the net current across the material:

$$\text{Equilibrium} \rightarrow \begin{cases} n_0 = n_i\,e^{(E_f - E_i)/k_B T} \\ p_0 = n_i\,e^{-(E_f - E_i)/k_B T} \\ J_n = \mu_n\,n_0\,\frac{dE_f}{dx} = 0 \\ J_p = \mu_p\,p_0\,\frac{dE_f}{dx} = 0 \end{cases} \tag{2.36}$$

If we inject hot carriers (electrons with energy above E_c) into the semiconductor, i.e. by a voltage application or by light illumination, we will be out of thermal equilibrium and we could not talk more about a Fermi level:

$$n = n_0 + \Delta n \tag{2.37a}$$

$$p = p_0 + \Delta p \tag{2.37b}$$

$$np \neq n_i^2 \tag{2.37c}$$

Although, one can define the electron and hole quasi-Fermi level in order to use the same expressions and notation as in equilibrium:

$$\begin{cases} n = n_0 + \Delta n = n_i\,e^{(E_{fn} - E_i)/k_B T} \\ J_n = \mu_n\,n\,\frac{dE_{fn}}{dx} \end{cases} \qquad \begin{cases} p = p_0 + \Delta p = p_i\,e^{-(E_{fp} - E_i)/k_B T} \\ J_p = \mu_p\,p\,\frac{dE_{fp}}{dx} \end{cases} \tag{2.38}$$

where, now, these quasi-Fermi levels are not equal, $E_{f_n} \neq E_{f_p}$.

This excess of carriers, when the equilibrium is broken by radiation exposition, can be taken into account through a carrier generation rate proportional to the light absorption in the material, generating (commonly) a non constant carrier concentration:

$$\frac{dn}{dt} = \frac{dp}{dt} = G \tag{2.39}$$

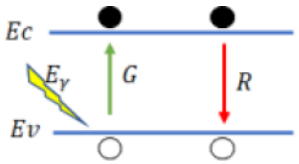

Figure 2.8: Representation of carrier generation and recombination in the semiconductor.

However, and in addition to the generation rate, when the equilibrium is broken the system tends to react in order to restore it. Thus, a recombination rate will appear as an attempt of compensate the external injection:

$$\frac{dn}{dt} = \frac{dp}{dt} = G - R \tag{2.40}$$

2.2.3 Generation of carriers

As we have mentioned, the generation rate will come from the absorption of the photons ($E_{ph} > E_g$) impinging the material. When passing through a solid, light's intensity (I) decay exponentially with the penetration depth (Beer-Lambert Law):

$$I(x) = I_0\, e^{-\alpha x}\ (W/cm^2) \tag{2.41}$$

where α is the absorption coefficient (cm^{-1}). Assuming that all the radiation losses are due to the semiconductor's absorption and, neglecting the presence of phenomenons involving multiple photons such as the two-photons absorption, the electron generation rate will be proportional to the decay density:

$$G(x) = -\frac{1}{E_{ph}}\frac{dI}{dx} = I_0\frac{\alpha}{E_{ph}}e^{-\alpha x} \tag{2.42}$$

Finally, as we are interested in the total generation produced in all the crystal and not only at a specific depth x, is convenient to take the average along the penetration depth:

$$\langle G\rangle = \frac{1}{w}\int_0^w G(x)\,dx = \frac{1}{w}\frac{1}{E_{ph}}I_0\ \left(1 - e^{-\alpha w}\right) \tag{2.43}$$

where $1/\alpha$ can be defined as the penetration length. If this length is much bigger than the solid height, a small amount of radiation will be absorbed, "Low injection". In the opposite, if $1/\alpha << w$ the radiation is heavily absorbed and the generation can be approximated to $\langle G\rangle \sim I_0/(E_{ph}w)$.

2.2.4 Recombination mechanisms

The recombination mechanism will act in the opposite way of generation, electron-hole pairs are annihilated when electrons of the conduction band recombine with holes in the valence band. There are three main types of recombination mechanisms: band-to-band, Auger and trap-assisted recombination.

Band-to-Band recombination

This is the dominant recombination mechanism for direct semiconductors that are not doped in excess. It is the simplest recombination mechanism; an electron of the conduction band recombines directly with a hole of the valence band, emitting a photon of the band gap energy. Thus, the recombination rate will be determined by the number of electrons found in the conduction band and the availability of holes in the valence band:

$$\mathcal{R} = \beta np \tag{2.44}$$

If we consider the case under thermal equilibrium:

$$\mathcal{R}_0 = \beta n_0 p_0 = \beta n_i^2 \tag{2.45a}$$

$$\frac{dn_0}{dt} = \frac{dp_0}{dt} = 0 \rightarrow \mathcal{R}_0 = G_0 \tag{2.45b}$$

Under equilibrium, the generation and recombination rates are driven by thermal fluctuations and must be equal in order to maintain constant the carrier density.
Then, out of equilibrium, the net recombination will be:

$$R = \mathcal{R} - G_0 = \beta(np - n_i^2) \tag{2.46}$$

If we consider a low injection state ($\Delta n << N_d$) , which is the most common situation, the recombination rate will be proportional to the minority carrier density. In the case of an n-type semiconductor:

$$\left\{ \begin{array}{l} n = n_0 + \Delta n = N_d + \Delta n \sim N_d \\ p = p_0 + \Delta p \end{array} \right\} \rightarrow R \sim \beta[N_d(p_0 + \Delta p) - N_d p_0] = \frac{\Delta p}{\tau_p} \tag{2.47}$$

with $\tau_p = \frac{1}{\beta N_d}$. being the electron/hole pair lifetime. We can see, in effect, how the recombination is limited by the minority carrier density. This is because the recombination requires one hole for each electron, and then, if we have a doped semiconductor with one carrier much more abundant than the other, we will run out of this last much earlier than the other, slowing down the recombination process. And, obviously, how more doped is the semiconductor easier is the recombination, i.e. the electron/hole's lifetime decreases.

Auger recombination

This second recombination mechanism involves three carriers instead of the two required for Band-to-Band mechanism. Thus, it will depend strongly on the doping level as it requires a much more crowded system, i.e. it will be the dominant recombination mechanism for heavily doped regions.

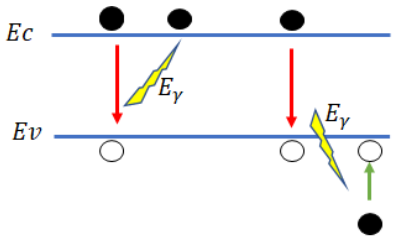

Figure 2.9: Representation of Auger recombination process.

This mechanism, in a similar way as the Band-to-Band, will consist on the recombination of an electron that drops from the conduction band with a hole at the valence band. The electron's de-excitation will emit a photon that, thanks to the high concentration of carriers, will be absorbed for a third carrier; an electron of the conduction band that will jump to higher states or an electron found in a relaxed state of the valence band that will occupy a hole at the valence edge. Then, in the first case, the recombination will depend quadratically on the electron's density, while in the second one, will depend quadratically on hole's density:

$$\mathcal{R} = c_n n^2 p + c_p p^2 n \tag{2.48}$$

If we consider the case under thermal equilibrium:

$$\mathcal{R}_0 = c_n n_0^2 p_0 + c_p p_0^2 n_0 = G_0 \tag{2.49}$$

Then, out of equilibrium, the net recombination will be:

$$R = \mathcal{R} - G_0 = c_n(n^2 p - n_0^2 p_0) + c_p(p^2 n - p_0^2 n_0) \tag{2.50}$$

Again, if we consider a low injection state ($\Delta n << N_d$) the recombination rate will be proportional to the minority carrier density. For the n-type case:

$$\left\{ \begin{array}{l} n = n_0 + \Delta n = N_d + \Delta n \sim N_d \\ p = p_0 + \Delta p \xrightarrow{p>>p_0} (p_0 + \Delta p)^2 \sim \Delta p^2 \end{array} \right\} \rightarrow \begin{array}{l} R \sim c_n N_d^2 \Delta p + c_p N_d(\Delta p^2 - p_0^2) \\ \sim c_n N_d^2 \Delta p + c_p N_d \Delta p^2 \\ \sim c_n N_d^2 \Delta p \end{array} \tag{2.51}$$

Effectively, this mechanism depends highly on the doping level, having a lifetime inversely proportional to the square of the doping density ($\tau_p = \frac{1}{c_n N_d^2}$).

Trap assisted recombination

For indirect semiconductors, a momentum supply is necessary in order to obtain the recombination of an electron/hole pair by means of the above two mechanisms. Thus, long lifetimes will be involved as it will be more unlikely to happen. Then, in this type of semiconductors, the dominant recombination mechanism is the trap assisted or SHR recombination. Here, instead of a direct annihilation of an electron of the conduction band with a hole at the valence band we have an energetic state inside the forbidden region of the band-gap that "catalyse" the electron/hole pair's recombination. These trap states are the result of the presence of imperfections in the semiconductor, like impurities or defects in the crystalline network, that facilitate the transfer of carriers.

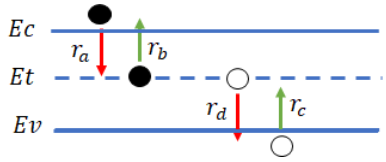

Figure 2.10: Representation of Trap assisted recombination process.

We can decouple the effect of this trap state over the electron and hole's density independently.

The amount of electrons that drop from the conduction band to the trap will be proportional to the electron's density and the amount of available sites in the trap level, i.e. the product of the total trap density states and the probability of being unoccupied, $N_t(1 - f(E_t))$.

$$r_a = v_{th}\sigma_n n N_t(1 - f(E_t)) \tag{2.52}$$

Also, the rate of electrons jumping to the trap will depend on their thermal velocity and on the strength of the trap influence (if the electron sees "close" or not the trap state) parametrized by the effective section, σ_n.

In the opposite, the amount of electrons that jump from the trap to the conduction band will be proportional only to the electron's density in the trap state. In this case, it is not necessary to take into account the amount of available states in the conduction band because we already know that it is practically empty and, then, it does not present any limitation.

$$r_b = e_n N_t f(E_t) \tag{2.53}$$

where e_n is the emission frequency (s^{-1}). With these two rates we know how the electron's density varies:

$$\frac{dn}{dt} = G - (r_a - r_b) \tag{2.54}$$

Proceeding in a similar way for the holes, we obtain that:

$$r_c = v_{th}\sigma_p p N_t f(E_t) \tag{2.55a}$$

$$r_d = e_p N_t(1 - f(E_t)) \tag{2.55b}$$

$$\frac{dp}{dt} = G - (r_c - r_d) \tag{2.55c}$$

Then, under thermal equilibrium ($\frac{dp_0}{dt} = \frac{dn_0}{dt} = 0$) and with no light ($G = 0$) the dropping and jumping velocities must be equal, imposing a specific value for the emission frequency of electrons and holes in the trap:

$$r_a = r_b \rightarrow e_n = v_{th}\sigma_n n_i \, e^{(E_t - E_i)/k_B T} \tag{2.56a}$$

$$r_c = r_d \rightarrow e_p = v_{th}\sigma_p n_i \, e^{(E_i - E_t)/k_B T} \tag{2.56b}$$

For simplicity, these emission frequencies will be considered valid for systems out of equilibrium. As an example, let's consider a semiconductor in a stationary regime:

$$\left.\begin{array}{l} \frac{dn}{dt} = 0 \rightarrow G = r_a - r_b \\ \frac{dp}{dt} = 0 \rightarrow G = r_c - r_d \end{array}\right\} \rightarrow r_a - r_b = r_c - r_d \tag{2.57}$$

As we are out of equilibrium, we cannot use any more the Fermi-Dirac distribution but playing with the equality found above and considering the emission frequencies of the equilibrium, one can extract a new probability density of having a state occupied at $E = E_t$:

$$f(E_t) = \frac{v_{th}\sigma_n n + e_p}{v_{th}\sigma_p p + e_n + v_{th}\sigma_n n + e_p} \tag{2.58}$$

Then, substituting this expression in the recombination rate, we obtain the general SHR recombination rate under stationary regime:

$$R = r_a - r_b = r_c - r_d = \frac{v_{th}\sigma_p\sigma_n N_t (pn - n_0 p_0)}{\sigma_p[p + n_i e^{(E_i - E_t)/k_B T}] + \sigma_n[n + n_i e^{(E_t - E_i)/k_B T}]} \tag{2.59}$$

And, if we consider the case of a low injection state, the minority carrier appears to be again the dominant term:

$$R \sim \frac{\Delta p}{\tau_p}, \quad \text{with } \tau_p = \frac{1}{v_{th}\sigma_p N_t} \tag{2.60}$$

With this result we can conclude that, as one could suspect, how higher is the absorption of holes to the trap higher is the recombination rate ($\Delta\sigma_p \rightarrow \nabla\tau_p \rightarrow \Delta R$).

Surface recombination

At the surface, due to the abrupt discontinuity generated at the lattice structure, there is a large number of recombination centers, N_t grow when we approach the surface. Thus, the recombination rate can be taken in terms of a surface recombination velocity ($cm \cdot s^{-1}$): $U_s = S\Delta p_n$. In the case of a n-type semiconductor under low injection, the recombination can be approximated to $R \sim \Delta p/\tau_p = v_{th}\sigma_p N_t(p - p_0)$. And, if we study the recombination occurring only in the surface, $R \cdot l = v_{th}\sigma_p N_t l(p - p_0) = v_{th}\sigma_p N_{t,s}(p - p_0)$, defining $N_{t,s}$ as the density of defects in the surface ($defects/cm^2$). With that, one can obtain the recombination current at the surface:

$$J_{rec} = qRl = qv_{th}\sigma_p N_t l(p - p_0) = qS\Delta_p \tag{2.61}$$

Even more, as the surface is the limit of our domain, the total current at it must be zero. Then, the diffusion current density of minority carriers is equal to the surface recombination rate:

$$qD_p \frac{dp_n}{dx}_{x=0} = qS\Delta p_n(x = 0) \tag{2.62}$$

2.2.5 Continuity Equation

At the end, if inside the semiconductor there exist a current, the final variation of the carriers density will be:

$$\begin{cases} \frac{dn}{dt} = G - R + \frac{1}{q}\frac{\partial J_n}{\partial x} \\ \frac{dp}{dt} = G - R - \frac{1}{q}\frac{\partial J_p}{\partial x} \end{cases} \tag{2.63}$$

knowing that these current can be generate by a gradient in the carrier concentration or due to the application of an electric field:

$$\begin{cases} J_n = qn\mu_n E + qD_n\frac{\partial n}{\partial x} \\ J_p = qp\mu_p E - qD_p\frac{\partial p}{\partial x} \end{cases} \tag{2.64}$$

and, that the recombination rate is the sum of three recombination mechanisms:

$$R = \frac{\Delta i}{\tau_i} \text{ with } \frac{1}{\tau_i} = \frac{1}{\tau_{bb}} + \frac{1}{\tau_{srh}} + \frac{1}{\tau_{aug}} \tag{2.65}$$

where i is the minority carrier density, $i = n$ for a p-type semiconductor and $i = p$ for a n-type semiconductor.

2.3 PN junction and the diode model

Since now we have considered at the same time only one type of semiconductor. But what happens when we have two semiconductors of different types in contact, i.e. a p-type semiconductor joined with an n-type? Here, as we have a region with a huge concentration of electrons in front of another poor in electrons, a diffusion of electrons will appear from the n-type semiconductor to the p-type.
Then, the thermal equilibrium is broken and the system will react to restore it. The charges that are transferred from one region to the other will fill the interface defects, neutralizing them and charging until a certain depth the two semiconductors. Thus, these charges will generate an electric field that will act in the opposite direction of the diffusion, creating a potential barrier (Built-in potential, V_{bi}) for the carriers transferred.

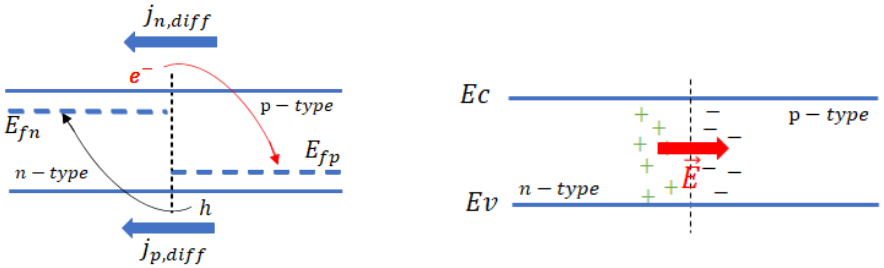

Figure 2.11: Initial out-of-equilibrium stages of a PN junction.

One can easily obtain the value of this potential barrier knowing that it will be the difference between the two initial Fermi levels. This is because, at the end, when the equilibrium is again reached, the Fermi level in both semiconductors must be the same but maintaining their p or n nature. Then, assuming room temperature, we obtain after some operations:

$$qV_{bi} = E_g - (E_c - E_{f_n}) - (E_{f_p} - E_v) \xrightarrow[n\sim N_d]{p\sim N_a} V_{bi} = \frac{k_B T}{q} ln\left(\frac{N_d N_a}{n_i^2}\right) \tag{2.66}$$

where k_BT/q is Einstein's relation: $D/\mu = k_BT/q = V_T$. This depletion in the bands is called space charge region and it's width ($W = x_p + x_n$) can be calculated from Gauss law, having in mind the charge neutrality condition.

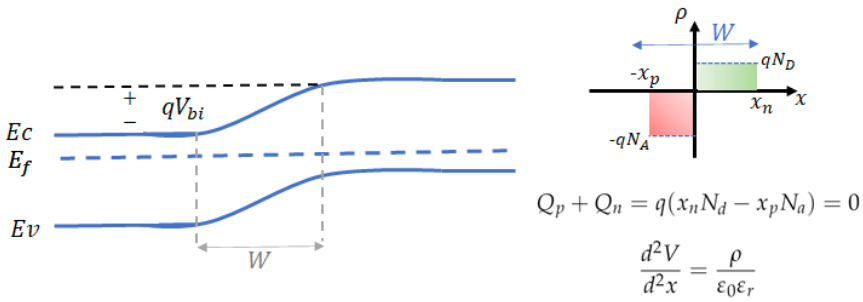

Figure 2.12: Built-in potential in PN junction and space charge width extraction by neutrality condition.

where ρ is the charge density ($-qN_a$ when $x \in [-x_p, 0]$ and qN_d when $x \in [0, x_n]$), ε_0 the vacuum permeability and ε_r the dielectric constant of the material. From the neutrality condition and knowing that $W = x_n + x_p$ one can find that:

$$x_p = W\left[\frac{N_d}{N_a + N_d}\right] \qquad \& \qquad x_n = W\left[\frac{N_a}{N_a + N_d}\right] \tag{2.67}$$

Thus, if one of the semiconductors is heavily doped compared with the other, practically all the tension fall will occur in the low doped region. Then, with the Gauss equation one can relate the built-in potential with the zone's width by:

$$W = \sqrt{\frac{2\varepsilon}{q}\left[\frac{1}{N_a} + \frac{1}{N_d}\right] V_{bi}} \tag{2.68}$$

If we apply a tension V over this junction, or diode, we will displace upward or downward the bands, increasing or decreasing the potential barrier. As convention, we take as reference node the n-type semiconductor. Then, when applying a positive tension, V>0, the bands of the p-type semiconductor will drop an energy qV and the potential barrier will be reduced, $q(V_{bi} - V)$, and the transfer of electrons to the positive node will be facilitated. Or in other words, the current will be increased when a positive tension is applied. If the voltage is negative, the barrier height will be increased and the flow of electrons will be minimized.

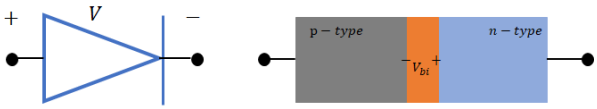

Figure 2.13: Diode symbol and conventional polarization.

After having studied the electrostatic of the PN junction, we can focus now into the I-V characteristics given by it. As we have already mentioned, the equilibrium is reached thanks to the suppression of the total current when an electric field appears to contrarest the diffusion of carriers:

$$J_p = J_{p,diff} + J_{p,drift} = 0 \rightarrow E = V_T \frac{1}{p}\frac{dp}{dx} = -\frac{dV}{dx} \rightarrow dV = -V_T \frac{dp}{p} \tag{2.69}$$

Thus, we can also write the built-in potential in terms of carrier concentration:

$$V_{bi} = -V_T ln\left(\frac{p_0(x_n)}{p_0(-x_p)}\right) \tag{2.70}$$

From this, we can obtain the minority carrier density at the onset of the absorber region:

$$p_0(x_n) = p(-x_p)\, e^{-V_{bi}/V_T} \sim N_a\, e^{-V_{bi}/V_T} \tag{2.71}$$

And, doing the same for the current of electrons:

$$n_0(-x_p) = n(x_n)\, e^{-V_{bi}/V_T} \sim N_d\, e^{-V_{bi}/V_T} \tag{2.72}$$

One may notice that this is the exact form of Boltzmann's distribution. As the number of available states is many orders of magnitude bigger than the carriers that try to occupy them, it will be very unlikely to have two carriers occupying the same state and, then, Boltzmann's formulation can be satisfied. So, the electron's density at the p-type border will be given by the amount of electrons in the n-type semiconductor that have the enough energy to jump the potential barrier, i.e. the probability of having an electron with energy equal to the barrier's height e^{-qV_{bi}/k_BT}.
If we apply an external potential, breaking the equilibrium, the barrier height will vary and these boundary conditions for the carrier's density will change:

$$n(-x_p) = N_d\, e^{-(V_{bi}-V)/V_T} \qquad \& \qquad p(x_n) = N_a\, e^{-(V_{bi}-V)/V_T} \tag{2.73}$$

and the excess of carriers will be given by:

$$\Delta n(-x_p) = n(-x_p) - n_0(-x_p) = N_d\, e^{-(V_{bi}-V)/V_t}\left[e^{V/V_T} - 1\right] = n_0\left[e^{V/V_T} - 1\right] \tag{2.74a}$$

$$\Delta p(x_n) = p(x_n) - n_0(x_n) = p_0\left[e^{V/V_T} - 1\right] \tag{2.74b}$$

Once we have the boundary conditions for the excess of carriers at both absorbing regions, we can use the continuity equation in order to find the I-V characteristics. If we suppose that the system is found at stationary regime and, then, that the total current is constant, we can calculate it at any point. For simplicity, we consider the point $x = x_n$ where the current will be the sum of both minority and majority currents: $J_T = J_n(x_n) + J_p(x_n)$.
For the minority one, we can assume that, as the electric field is small, the drift current contribution is negligible. Then, we have that $J_p(x_n) \sim J_{p,diff}(x_n) = -qD_p\frac{d(\Delta p)}{dx}$ and applying this to the continuity equation for holes under stationary regime ($\frac{dp}{dt} = 0 = G - R - \frac{1}{q}\frac{dJ_p}{dx}$) and solving for a long domain (the diffusion length, L_p, is smaller than the wafer material's length), we find an excess carrier concentration of

$$\Delta p(x') = \frac{n_i^2}{N_d}\, e^{-x'/L_p}\left[e^{V/V_T} - 1\right],\ \textit{where } x' = x - x_n \tag{2.75}$$

and with that, a hole's current in the n region of:

$$J_p(x_n) = -qD_p\frac{d(\Delta p(x_n))}{dx} = qn_i^2\frac{D_p}{N_d L_p}\left[e^{V/V_T} - 1\right] \tag{2.76}$$

To find the electron's current at x=xn we suppose that it will be the same as the current in $x = -x_p$ as there is no generation by radiation exposition and the space charge

region is narrow enough to neglect the existence of recombination. Thus, $J_n(x_n) = J_n(-x_p)$, and as in $x = -x_p$ the electron's current is the current of minorities we can proceed in a similar way as before, neglecting the drift component and a long wafer:

$$J_n(x_n) \sim J_n(-x_p) = -qD_n \frac{d(\Delta n(-x_p))}{dx} = qn_i^2 \frac{D_p}{N_a L_n} \left[e^{V/V_T} - 1\right] \tag{2.77}$$

Then, we get that the total current for an ideal diode is:

$$J_T = J_n(x_n) + J_p(x_n) = qn_i^2 \left(\frac{D_n}{N_a L_n} + \frac{D_p}{N_d L_p}\right) \left[e^{V/V_T} - 1\right] = J_0 \left[e^{V/V_T} - 1\right] \tag{2.78}$$

However, if we try to be more accurate in order to modelize a real diode we should take into account a non-null recombination current in the space charge region. Considering a recombination mechanism assisted by traps and taking the simplifications of assuming a trap energy level close to the intrinsic Fermi level, the same effective section for electrons and holes, and a small carrier concentration ($n, p << n_i$), we obtain an additional diode current of the form:

$$J = J_{ideal} + J_{scr} = J_0 \left[e^{V/V_T} - 1\right] + J_{02} \left[e^{V/(2V_T)} - 1\right] \tag{2.79}$$

with $J_{02} = qn_i W/(2\tau_{scr})$. Depending on which diode dominates we can write a simplified expression for the current:

$$J = J_s \left[e^{V/(nV_T)} - 1\right] \tag{2.80}$$

being n the ideality factor of the diode. In addition, during the fabrication process it can appear defects, such as pinholes, that introduces a series and parallel (or shunt) resistanceS to the equivalent circuit:

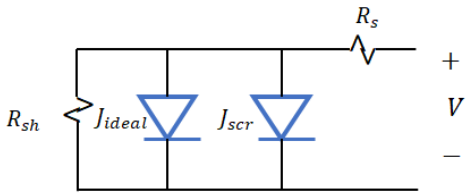

$$J = J_s \left[e^{(V - R_s J)/(nV_T)} - 1\right] + \frac{V - R_s J}{R_{sh}}$$

Figure 2.14: Equivalent circuit and current for a non-ideal diode.

2.4 Solar Cells

2.4.1 Absorber and selective contacts

When we submit a semiconductor under a light exposition, a photocurrent is generated in its bulk, J_{ph}. For a photodiode, or solar cell, the final current expression takes the form of $J = J_0 \left[e^{V/V_T} - 1\right] - J_{ph}$. However, in order to collect and extract the generated current, only with a PN junction is not enough. A separation of carriers must be done to avoid their recombination in the external circuit. Thus, a solar cell consists of an absorber bulk that generates a photocurrent and two selective contacts that collect electrons (ETL) on one side and holes (HTL) on the other.

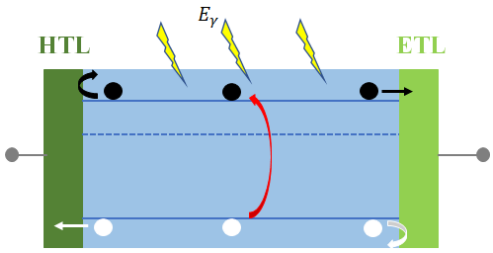

Figure 2.15: Schematic representation of solar cell's work principle: Absorber + Filters

Before explaining the different strategies to obtain a selective contact, we introduce here the concept of Electrochemical potential as a driving force in the transport of carriers. Recovering the carrier transport expressions obtained in the previous chapters:

$$J_n = qn\mu_n E + qD_n \nabla n \tag{2.81a}$$

$$J_p = qp\mu_p E - qD_p \nabla p \tag{2.81b}$$

and knowing that the electric field is the gradient of the electric potential, $E = -\boldsymbol{\nabla} V$, and that the chemical potential of one carrier type is defined as $\Psi_{chem,i} = \Psi_{chem,i_0} + k_B T ln(i/i_0)$, with $i = n$ or p, and using Einstein's relation, $D_i = \mu_i k_B T/q$, one can rewrite the currents as:

$$J_n = -\frac{\sigma_n}{q}\nabla(qV) + q\mu_n k_B T n \frac{\nabla n}{qn} = -\frac{\sigma_n}{q}\nabla(qV) + \frac{\sigma_n}{q}\nabla\Psi_{chem,n} = \frac{\sigma_n}{q}\nabla\eta_n \tag{2.82a}$$

$$J_p = ... = \frac{\sigma_p}{q}\nabla\eta_p \tag{2.82b}$$

where $\eta_n = \Psi_{chem,n} + qV$ is the electrochemical potential for electrons and, in semiconductor physics, is equal to the electron's quasi-fermi level. This can be easily checked by comparison of the current expressions found in Eq. 2.44 and the one above.
Thus, the electrochemical potential is the driving force behind current in semiconductors and, the carrier conductivity, σ, is the material property determining the reaction level of carriers to this force. Also, these expressions tell us that holes move to higher values of electrochemical potential (to negative domains), while electrons drop to lower values, tending both to their more relaxed states.
With this, a selective contact can be reached via two main strategies. Directly separation of carriers by the introduction of energy barriers that blocks one carrier's type while promotes the flow to lower energies for the other, or, through dissimilar conductivities between electrons and holes, i.e. $\sigma_n \neq \sigma_p$, where one conductivity is much bigger than the other, restricting the transport of this last one.
From Schottky theory, one can achieve carrier selectivity applying directly over the semiconductor metal layers with asymmetrical work functions in order to manipulate the surface potential of the semiconductor, and obtain regions of accumulation and depletion that separate the carriers.
If we contact a metal with high (small) work function, i.e. 3 eV (when the silicon affinity is of the order of 4eV), the electrons of the metal will see in the conductive band of the semiconductor available states with more relaxed energy, dropping into them and, then, doping the absorber surface with n-type character as the electrochemical potential is tuned. With this n-doping we curve the bands and increase the electron conductivity, selecting preferentially these carriers. But, in reality, indistinctly of which metal (work function) we have contacted, the concentration of carriers at the

semiconductor surface remains unchanged, we always obtain a Schottky barrier at the metal-semiconductor junction. This is called "Fermi Level pinning" (FLP), and can be attributed to the formation of a high density of states in the mid-band gap of the silicon due to the surface dangling bonds that act as tramps. The most affordable solution to Fermi level pinning is to dope the semiconductor surface in order to narrow its width ($W \sim N_d^{-1/2}$), allowing the quantum-mechanical tunneling of the carriers. But, increasing the doping level also increases the Auger-recombination rate.

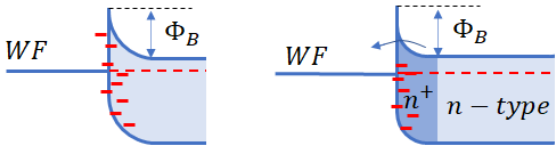

Figure 2.16: Metal-semiconductor junction without and with a heavily doped semiconductor's interface.

An advance to this is to introduce a passivation interlayer, which apart from passivating the semiconductor surface reducing the number of defects and dangling bonds, separates the silicon from the metallic layers avoiding the emergence of additional states inside the band gap, suppressing the FLP effects. One example is to interlay a thin film consisting of a wide band gap insulating dielectric such as SiO_2, Al_2O_3 or TiO_x between the semiconductor and the metal terminal that passivates the semiconductor's surface defects, being thin enough to allow the transport of the majority carrier through tunneling, and that when the band alignment is done it will present a huge barrier for the minority carriers thanks to its wide band gap. [19, 20].

Figure 2.17: (a) Metal-insulator-semiconductor and, (b) Field-Effect passivation contact diagrams (ETL).

Alternatively, we can perform a selective contact that also passivates the semiconductor surface by the use of the so-called "Field Effect Passivation". As in non-intrinsic regions the recombination is governed by the minority carrier, reducing the amount of this will also decrease the recombination. We can perform this reduction via an electric field introduction (thanks to a dipolar[21] or charged interlayer[22]) that attracts in major one of the two carriers varying the electron/hole ratio. Thus, both Auger and FLP issues are attenuated while selecting one carrier.

2.4.2 Solar cell's parameters

As we have said previously, the IV curve of a solar cell under light exposition is the superposition of the diode current (called "dark" current) and a light-generated current (also called photocurrent, I_L) that shifts the IV curve into the fourth quadrant:

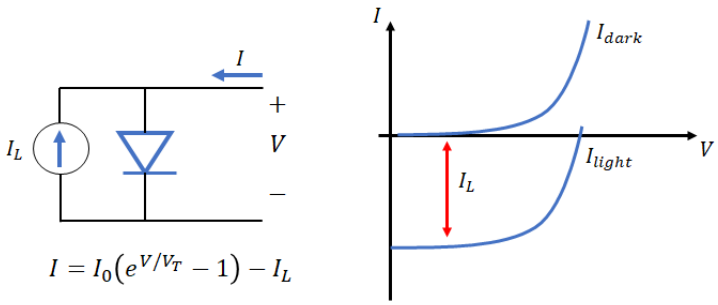

Figure 2.18: Ideal solar cell equivalent circuit and IV curve.

Thus, as the current is not null, one can extract power from the diode. This total power can be calculated as the area of the rectangle formed by the shifted IV curve and the axes of the fourth quadrant. However, the IV curve is normally set in the first quadrant in order to work with positive powers:

$$I = I_L - I_0 \left(e^{V/V_T} - 1\right) \tag{2.83}$$

With this curve, one can extract some of the most important characterization parameters for a solar cell. For instance, one may know the point where the output power makes maximum, P_{max}, as it should be the work point of our device. This can be obtained seeking for the point that makes zero the derivative of the current and voltage product: $\frac{d(VI)}{dV} = 0$.
Apart from the power, one may highlight the short-circuit and open-circuit points. In the first one, where the voltage across the cell is null, the current given by the solar cell will, entirely, come from the generation and collection of the photocurrent. Thus, the short-circuit current (I_{sc}) is an indicator of the absorption behaviour of the cell (the higher collection probability the higher I_{sc}) and of the resistive loss mechanisms present in the device, being equal to the light-generated current in the ideal case. In contrast, the open-circuit voltage, where the current is zero, indicates the bias of the diode junction under light exposition and it depends logarithmically with sunlight intensity (considered towards the photocurrent): $V_{oc} = \frac{nk_BT}{q} ln\left(\frac{I_L}{I_0} + 1\right)$.
Knowing that the short-circuit current and the open-circuit voltage are, respectively, the maximum current and voltage that the solar cell can provide, one can estimate how far our device is from the ideal power supply defining the Fill Factor (FF). This parameter is the ratio between the maximum power extracted for the solar cell and the product of V_{oc} and I_{sc}: $FF = \frac{P_{max}}{V_{oc} Isc}$.

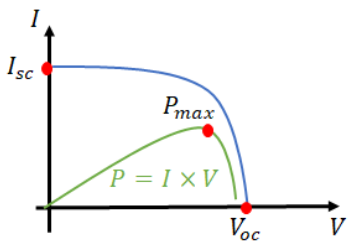

Figure 2.19: Figure containing the most relevent parameters for a solar cell.

If we have a bad passivation of the metal-silicon interface, we can have that non-collected carriers recombine at the contact as both electrons and holes can reach with

similar facility the mid-gap defect and, then, a loss in the electrochemical potential of the systems will be obtained (drop in the V_{oc}). In a different way, the fill factor (FF) is affected by the majority current passing through the contact, and then, by the contact resistance as FF tells us how close from the ideal we find our device.
Besides the Fill Factor, the short-circuit current and the open-circuit voltage, one of the most commonly used parameter to qualify the performance of a photovoltaic device is its efficiency. This parameter compares the power obtained by the solar cell with the input power supplied by the incident light. The convention is to use as incident light the AM1.5 solar spectrum which assumes that the sun light passes through 1.5 atmospheres, taking into account the non-normal incidence of the solar radiation at mid-latitudes regions. By integrating all the wavelengths, the total incident power given by the AM1.5 spectrum has an approximately value of $1000W/m^2$, and the efficiency can be written as: $\mu = \frac{Pmax}{Pin} = \frac{V_{oc} I_{sc} FF}{1000W/m^2}$.
In addition, one may note that the efficiency is highly dependent on the semiconductor's bandgap. If we have a semiconductor with a wide bandgap, only high energetic photons could be absorbed, wasting most of the solar spectrum. In contrast, if the bandgap is narrow we will absorb all the incident photons (at least the ones that are not reflected) but part of the energy absorbed by the electron will be lost in the form of heat when falling to the conduction band. This effect was firstly considered by Shockley & Queisser (1961) and limits the c-Si based solar cells' efficiencies below the 44%.

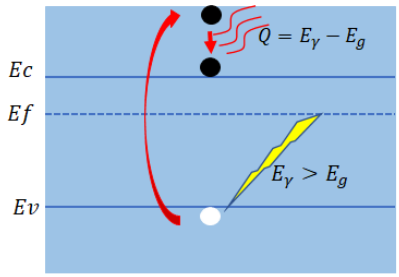

Figure 2.20: Thermal losses in high energetic photons absorption.

Deeply, to characterize the selective contacts operation we use two main parameters: saturation current contribution from contact recombination, $J_{o.c}$, and the contact resistivity ρ_c. The first one, tells us how important is the recombination at the interface and then the passivation quality that at the end determines the losses in the open circuit voltage. In contrast, the contact resistivity tells us the resistance that the carrier will find when they are extracted and, then, how close we are from the ideal case. It can be defined as $\lim_{V \to 0} \frac{V}{J}$. [23].
Obviously, not all the photons that impinge the semiconductor will be absorbed. We have to take into account the loss mechanisms, such as reflection of photons or recombination of electron/hole pairs, that limit the generated photocurrent. The parameter considering these losses is the external quantum efficiency (EQE), which is defined as the number of electron/hole pairs generated per incident photon. Ideally all the photons with an energy higher than the semiconductor's band gap ought be absorbed, the $EQE_{ideal}(\lambda) = 1$ at those wavelenghts $\lambda < \frac{hc}{E_g}$. However, due to recombination mechanisms the quantum efficiency is reduced, and one can understand the EQE as the probability of collecting a carrier generated by a photon of a certain wavelength.

2.4.3 PEI as selective contact

We have mentioned above that in c-Si based solar cells the more limiting factors in their crucial parameters, Voc and FF, which determines the efficiency and viability of our devices are carrier selectivity and recombination losses. These makes of selective contacts research a highly important topic in the development of high efficiency photovoltaic technologies. This kind of contacts accomplish the mitigation of both limiting factors. Thus, in this section we will introduce the basic concepts and work principles of the selective contacts employed along this project: Polyethylenimine (PEI).
In the industry, the widely implemented c-Si photovoltaic technology applies directly the contacting metal onto the absorber semiconductor, what leads to many issues, being, as we have already seen, the Fermi-Level Pinning the most relevant one. This phenomenon deeply constrains the efficiency of direct contacted devices. The most common strategy in order to overcome FLP is to narrow the Schottky's barrier width by doping heavily the semiconductor surfaces, allowing the quantum-mechanical tunneling through this. This technique gives us high efficiency solar cells of ($PCE > 24\%$ [24, 25]) and it is easily applicable for industry, but as the doping process requires high temperature and long duration steps [26] in order to diffuse the dopant into the semiconductor, many efforts has been invested in the research of simpler and less costly diffusion steps [27, 28] or free-doping contacts. In the context of this last one, incorporation of organic thin films between the metal-semiconductor contact, such as conjugated polymers, has emerged as promising alternatives [29].
These thin films do the function of dipolar layers that apart from passivating the surface defects drag carriers from the metal contact to the semiconductor through their dipolar moment, modifying the metal's work function and obtaining a doped surface without the necessity of carrying a thermal diffusion process [30, 31]. There are many examples of these organic molecules or self-assembled monolayers in the literature, having PEDOT:PSS an special success [32] regarding it's issues with respect to long term stability. In our work we have focused in the study of polyethylenimine (PEI) as dipolar layer over different absorbers. All these will be explained in more detail in the experimental part of this work.
Other dopant-free contacts, which are worthy to mention, are those based on the use of heterojunctions of the absorber with high band gap materials. In this subcategory metal or transition metal oxides, such as TiO_x, MoO_x, indium tin oxide (ITO) or vanadium oxide (V_2O_x) [33, 34, 35], appear to be the more matching materials with a wide range of work functions and refractive indexes, fact that support their use as frontal contacts. Additionally, the possibility of depositing them through low-temperature processes like physical vapour deposition or sputtering reduces the final cost of the cell.

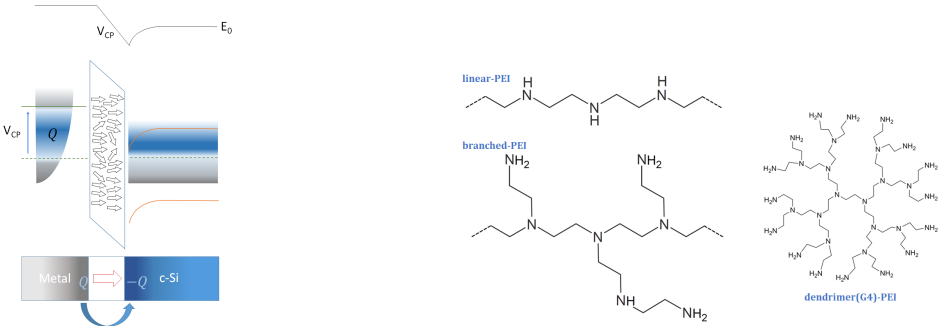

Figure 2.21: (Left) ETL contact enhancement by the dipolar effect of CP pendant groups (Source: Eloi Ros Costals) and, (Right) different PEI structures

In the case of conjugated polyelectrolytes as selective contacts, they can be deposited via low-temperature, economical and large-scale manufacturing processes either in solution (roll-to-roll [36] and spin-coating [37]) or gas form (thermal evaporation) [38]. These organic layers have been widely studied in the field of organic photovoltaics and electronics, specially in OLEDs applications, and their good performance as selective layers has been attributed to the presence of polar or charged pendant groups in the molecule structure that generates a dipolar electric field in the metal-semiconductor interface improving the injection of carriers from the electrode to the absorber [30]. Thus, the semiconductor's surface is doped via a Field-Effect mechanism what increases the conductivity of the injected carrier, improving the contact selectivity, and the voltage associated to the dipole modifies the electrode's work function (reducing, or increasing, it if we have an ETL, or a HTL) improving the Schottky's contact.
The principles behind the use of PEI is similar to the more frequently reported use of PFN. Here, the high number of amino groups present in these molecules and their Lewis basicity give them a high cationic behaviour. Then, under dissolution with some alcohol the amine groups protonate, facilitating their linkage with the counterions present in the solution that will arise a non-null dipolar momentum. However, this kind of conjugated polymers have a very low conductivity and, then, they must be deposited in enough thin layers in order to allow the quantum-tunneling transport. Apart from the common benefits of dopant-free contacts based on CPs, what advantage the use of polyethylenimine is its long background in the chemical and biotechnology industry thanks to its application in paper fabrication or genetics engineering as a DNA transfection agent [39, 40]. Also, as it can be synthesised in different structures, from linear to fractal passing through hyperbranched [41, 42], one can vary the strength of the dipolar layer by varying the amount of surface amino groups, giving us a great versatility depending on the desired specifications for our device. In our project, we will work with branched-PEI but, to simplify notation, we will refer to it simply as PEI.

2.5 Thin film solar cells (TFSC)

Until now, we have focused the main theory over silicon based solar cells. It has been done on purpose as this technology dominates more than 90% [5] of the photovoltaic market with high efficiency devices (commercially between 14-20% but with reported efficiencies over 25% [43]) and with simple and largely consolidated theory behind it. However, due to the large amount of silicon necessary to obtain high absorbent and efficient devices, with wafers of $300\mu m$ thick in the case of mc-Si, high costs are associated to this technology, either economical (the extraction and fabrication of silicon wafers represent more than 50% [44] of the total module cost) and geopolitical, where China is the major producer of raw silicon ($> 60\%$ [45]) and PV modules ($\sim 80\%$ [46]). Thus, a lot of research has been invested in order to find a suitable photovoltaic technology away from silicon. All these technologies can be classified into four generations of solar cells, being the silicon ones the first generation [47]:

- **Second generation or thin film:** Based on direct band gap semiconductors what enables them to heavily reduce their widths, being amorphous hydrogenated silicon (a-Si:H), copper indium gallium sulphide (CIGS) and cadmium telluride (CdTe) their maximum exponents. They reduce the economical costs, but with lower efficiencies compared to silicon cells.

- **Third generation or organic:** Based on small molecules or thin-film polymers of high bandgaps. They present a more complex operation where, instead of the band theory and p-n junction, they work with molecular orbital overlappings and Acceptor-Donor structures. Among their benefits, highlight the simple, low-temperature, and cheap fabrication steps like spin coating or roll-to-roll processing. However, they are still limited by stability and degradation issues.

- **Fourth generation or tandem:** This generation of solar cells was borned due to the necessity of increasing the efficiency of silicon solar cells. They consist of the so-called "multijunction" approach, where layers of different band gap materials are stacked in order to absorb the maximum percentage of the incident radiation.

In addition, as the main goal of our work is to investigate PEI selective contact into different thin film absorbers (concretely, kesterites and antimony selenide), it is worthy to enter in more details about the second generation of solar cells.
Some literature highlights the difference between "thin" and "thick" films [48]. Both are layers of widths between a few nanometers to tens of micrometers and the structural, electrical and optical properties of both films are extremely dependent on their thickness, but they are distinguished because of their different fabrication mechanisms. The first ones are materials created from scratch (ab initio) where monolayer by monolayer the film is grown, such as atomic layer deposition (ALD) or chemical bath deposition (CBD). The fact of growing our material from the beginning gives us an effective control on the final film's properties, from their crystallinity and orientation to their phases. In contrast, thick films are obtained from a macroscopic material target, either perfilling it or depositing clusters pulled up from a target by a plasma or by ablation. Although being more aggressive and inaccurate deposition mechanisms, they offer a cheaper and simpler way of obtaining thin materials.
Then, thin-film solar cells offer a great variety of deposition techniques, making them a high versatile technology. The most commercially extended thin-film solar cell is amorphous silicon technology which had a rapid growth in the late 1980s. The implied low-temperature deposition techniques and the reduced amount of silicon made of it a promising candidate for photovoltaics, but due to their lower efficiencies and stability problems (with stabilised module efficiencies normally ranged between 4-6%) it was eclipsed by the advances in c-Si solar cells. However, thanks to the enhancements reached in recent years via multijunction cells with hydrogenated amorphous silicon (a-Si:H), what reduces the presence of dangling bonds and helps to improve the minority carrier length, and amorphous silicon alloyed with germanium (a-Si:Ge), which has exhibit to reduce the Staebler-Wronski light degradation effect linked to the latter hydrogenation, this technology has recovered part of the PV market.[49, 50]
Due to amorphous silicon's light degradation issues, CIGS and chalcogenide-based (specially CdTe) solar cells emerged as promising alternatives. The first one consists on metal alloys, with typical stoichiometry $Cu(InGa)(Se,S)_2$, deposited by elemental evaporation or sputtering techniques, while the second one can be deposited via chemical bath deposition. But, as both absorbers have a multicrystalline structure, grain sizes, secondary phases and plane orientation highly determines the device performance.
Although both technologies have overpassed efficiencies of the 21% [51, 52] in laboratory conditions, they carry important environmental troubles due to the use of critical raw materials (CRMs) such as indium and toxic materials like cadmium. That is why many efforts are being invested in the seek of new materials for the next generation of thin film technologies, where Perovskite, Copper zinc tin sulfide (CZTS) or Antimony selenide (Sb_2Se_3) are the most promising ones.

2.5.1 Kesterite solar cells

Kesterite based solar cells emerged as a CRM-free alternative to CIGS thin-film photovoltaics, where no indium or gallium is employed. They are a full inorganic alloy composed of copper, zinc, tin and selenium or sulphur ($Cu_2ZnSn(S,Se)_4$) typically abbreviated as CZT(S,Se). Actually, kesterite is the name given to the most stable phase of CZT(S,Se), different to the other two main phases: stannite and mixed Cu-Au. Apart from not involving critical raw materials, kesterites have some properties that make them a promising technology for the photovoltaic industry. Firstly, their compounds are metals very widespread in the metallurgic industry such as bronze. Thus, there already exists an industry network used to work with these materials. And, secondly, although kesterites based solar cells are still young, they started to be renown in the beginnings of the 2010s decade even though the first PV device appeared at 1997 [53], as they have a similar structure to the CIG(S,Se) family, replacing $2In^{+3}$ or $2Ga^{+3}$ by $Sn^{+4}Zn^{+2}$, many of the strategies followed in this "older" family (finals of the 70s [54]) can be transferred to kesterites.

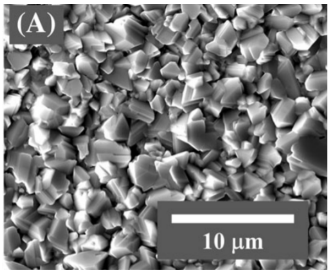

(a)

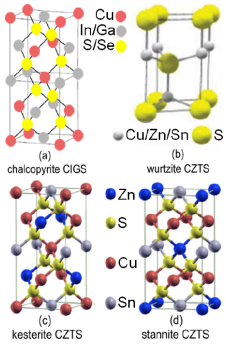

(b)

Figure 2.22: (a) SEM image of CZTSe surface [55] and, (b) Crystal structures of CIGS and CZT(S,Se) phases [56].

In spite of this absorber' suitable properties for thin-film photovoltaic applications, with band-gaps ranging from 1eV to 1.5 eV, respectively, for selenide and sulphide kesterites, its high light absorption coefficient ($\sim 10^5 cm^{-1}$) and their intrinsic p-type conduction; kesterites have associated important limiting factors and difficulties, which are the responsible of obtaining efficiencies much below than the ones reachable with CIGS technology (in the range of 11-13%). High defects density, presence of undesired secondary phases generated during the synthesis process, high surface roughness ($\sim 100nm$), in-homogeneous composition or fractures/pin-holes due to their polycrystalline structure are the most unsettled ones. [57]
In order to deal with the presence of secondary phases and bulk traps in the kesterite, intrinsic doping is typically carried out. We refer to intrinsic doping as the variations in the alloy' stoichiometry by enriching or impoverishing the kesterite with some of its compounds. This process is done during the kesterite synthesis.
Nowadays, the most widely used strategy to grow kesterites is the so-called two-step process in which a first precursor film deposited by sputtering, evaporation or PLD contains all the chemical elements (aggregated in binary or ternary species like Cu_2X or Cu_2SnX_3, with X=S or Se) necessary for the absorber formation, and, then, a thermal annealing treatment under S (sulfurization) or Se (selenization) containing atmosphere is performed in order to grow the kesterite grains. We have pointed out the necessity of using binary or ternary species for our precursor film because when the annealing

step is performed, the higher stability of metal-chalcogen species, i.g. ZnX, compared with the quaternary kesterite phase would make it practically impossible to obtain the absorber. Thus, the two main path-ways to synthesise kesterites are the nexts:

$$Cu_2X(s) + ZnX(s) + SnX(s) + \frac{1}{2}X_2(g) \leftrightarrow Cu_2ZnSnX_4(s) \tag{2.84a}$$

$$Cu_2SnX_3(s) + ZnX(s) \leftrightarrow Cu_2ZnSnX_4(s) \tag{2.84b}$$

As we can see, we have to form in a first stage a ternary alloy without zinc and add a posteriori the zinc through the ZnX to form the kesterite. However, and due to the high stability of this metal-chalcogen species, the kesterites obtained by these processes will be poor in zinc making necessary a zinc-dopage in some regions of the absorber in order to assure the complete reaction of all the reactants and avoid the presence of secondary phases (Cu_2SnX_3, Cu_2X,...) in the kesterite.
Then, modifying the ratios between these ternary and binary precursors we can obtain different compositions for the kesterite (normally, off-stoichiometric kesterites). It has been found that the absorbers with highest efficiencies are the ones classified as type A: Cu-poor and Zn-rich. The last one is necessary to obtain a high-quality kesterite with small secondary phases, while the first one is related to the dopage level. Similarly to CIGSSe, the copper vacants have a preponderant role in the intrinsic doping level of our semiconductor, acting as shallow acceptor impurities.[58]
Nevertheless, it is difficult to obtain a well-performance kesterite even though we know the optimal configuration. The high sensitivity of the synthesis process on environment conditions, such as pressure or temperature, and on the order of deposition of the precursor materials, generates a high density of micro- or nanoscale fluctuations in the composition. These different domains can lead to internal electric fields formation and variations in the band gap, which will end up in losses in the solar cell performance, specially in the open-circuit voltage. And, additionally, the high volatility of Sn-chalcogenide species facilitates the release to the atmosphere of superficial tin when the kesterite is resting, obtaining Sn-poor surfaces.
One way to diminish the defects related with the complexity of the kesterite synthesis is the extrinsic doping, where other elements apart from the conventional ones are added to the alloy occupying vacants or replacing some of the initial elements. The two most promising ways of extrinsic doping involve the use of alkaline elements (Li, Na, K, etc.) and of isoelectronic elements from the same family of the elements of the initial composition ($Cu \rightarrow Ag$; $Zn \rightarrow Cd$;$Zn \rightarrow Ge$). And, within these strategies, the doping with Na and Ge, respectively, seems to be the more extended [59].
Finally, and after this brief summary of kesterite's absorber properties and limiting factors, it is worthy to discuss a bit the second wheel necessary to obtain a functional solar cell: selective contacts. There exist, for both hole and electron transport layers, predominant architectures which have been perfected and optimized over time and that now are difficult to alter.
The typical rear is a soda-lime glass substrate where a Molybdenum trilayer is deposited via sputtering. This trilayer configuration minimizes the overselenization of the rear contact during the thermal annealing while keeping reasonable electrical features. This is done in order to have only a thin $MoSe_2$ layer generation through Se diffusion when the annealing is done as it is predicted to improve the band alignment compared with pure Mo, being an excellent hole transport layer. The first, and widest, layer is a Mo synthesized under low pressure which gives it a great conductivity but also a high susceptibility to selenize. To protect it, a second layer of Mo is generated under a higher pressure which hinder the Se reaction but impoverish the conductivity.

Finally, a sacrificial layer of Mo sputtered under an intermedium pressure is deposited in order to be the Mo layer that reacts with the Se forming the HTL of $MoSe_2$.
However, the disposition and orientation of the $MoSe_2$ layers is crucial because a bad alignment can introduce a hole barrier potential. Additionally, the direct contact of the kesterite with the Mo can lead to some extra troubles. Decomposition reactions can be generated at the Mo/kesterite contact interface generating secondary phases as CuSe, ZnSe, SnSe and $MoSe_2$, introducing a high void density due to the volatility of some of these products. To mitigate this surface instability, one can isolate the kesterite from the Mo introducing an oxide in between, typically exposing the molybdenum substrate to the atmosphere during a long period in order to grow a native MoO_x. [60]

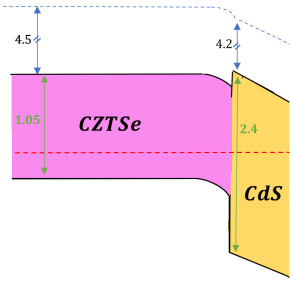

Figure 2.23: CZTSe/CdS spike-like conduction band alignment.

Regarding the ETL/window heterojunction, one must be very thorough with the conduction band alignments at the interfaces. A high-performance solar cell is obtained if a Spike-like alignment on the conduction band is obtained in the heterojunction (see Figure 2.25). That is because when a forward bias is applied the barrier is reduced and the injected carriers can pass easier over it. Then, a reduction in the recombination of majority carriers is obtained thanks to the lower blocking effect of the barrier which makes the dropping to interface defects more unlikely to happen. In contrast, if we have a Cliff-like band alignment the effect will be the opposite. The barriers for the injected electrons will increase as well as the recombination rate. Thus, in order to extract a good open-circuit voltage (V_{oc}) it is necessary to have a Spike-like alignment.
However, the conduction band offset of this Spike-like alignment should not overpass the +0.4eV because, otherwise, the "notch" formed will act as a barrier against the photogenerated electrons, leading to a reduction of the collected current (low J_{sc} and FF).
With all these, it has been widely reported that the most optimal ETL for kesterites [61] is a CdS layer, which accomplishes the required spike-like alignment and has a conduction band offset in the range of 0.33 - 0.48 eV depending on the deposition technique employed [62]. However, the use of a layer containing cadmium goes against the kesterite's raison d'être: give an alternative to TFSC involving critical raw materials. That is why new efforts are being invested in the research of cadmium-free ETLs, such as our CP based contacts.

2.5.2 Antimony sulfide-selenide solar cells

This second absorber can be classified as a binary metal chalcogenide semiconductor and solve all the lacks and troubles associated with the earlier thin-film absorbers. Similarly to kesterites, antimony sulfide-selenide is a semiconductor whose compounds are non-toxic, CRM-free, i.e. earth abundant as their availability in the earth crust is in the order of 0.2ppm, 260ppm and 0.05ppm for Sb, S and Se compared with the 0.005ppm of Te [63], and has a low environmental impact (low-temperature processes

thanks to its low melting points, 550ºC and 608ºC for Sb_2S_3 and Sb_2Se_3 respectively, and they crystallize at low temperatures, <350ºC). Moreover, this absorber presents a single stable phase, which represents a great improvement with respect to the appearance of undesired secondary phases in kesterites, and can be entirely synthesised through chemical bath deposition method.[64]
The most common method to synthesise this absorber is by chemical bath deposition (CBD), although co-evaporation is also employed, and consist on the immersion of a substrate (soda-lime glass or some plastic substrate if we desire a flexible device) inside a solution containing all the non-metallic precursors where the nucleation and particle growth of our material is obtained. This mechanism is very suitable for industry scale, as one can cover a large-area or carry a continuous deposition along a mobile substrate, in addition to its simplicity and low-damaging interaction [65]. There have been studied many different reactions and precursors in order to obtain the final antimony sulfide-selenide films, but the ones whose films appear to be more advantageous, specially for their crystallinity, use $SbCl_3$ as source of Sb^{3+} ions dissolved in acetone and concentrated $Na_2S_2O_3$ (or $CSe(NH_2)_2$) as S^{2-} (or Se^{2-}) ions source.

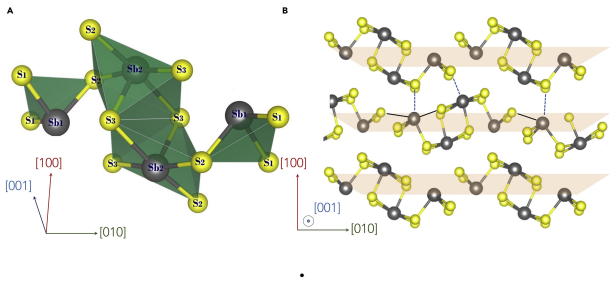

Figure 2.24: Antimony selenide crystalline structure, with ribbons and sheets [64]

In addition, due to the great sensitivity of chemical bath deposition towards the solution conditions (bath temperature, pH, molarity, etc.), the electrical and optical properties of the semiconductor can be altered. Experimentally has been obtained band gaps in the range of 1.3-2.2eV which makes antimony sulphide-selenide a wide band-gap absorber suitable for tandem applications as top subcells [66, 67]. However, for high-performance solar cells one may take into account the crystalline structure of the antimony sulphide-selenide because its preferential orthorhombic crystal structure give to it a chain-like structure, with ribbons and sheets, that leads to an anisotropic electrical conductivity [68]. Thus, depending on the orientation of the crystalline planes the charge transport can vary affecting, at the end, the solar cell performance. Also, due to the lowest surface energy and the presence of no covalent bond breakage, orthogonal planes to [0,0,1] are the most likely to be formed at the semiconductor surface, leading to a low number of dangling bonds and a clean band gap what makes of this absorber stable and low reactive to the atmosphere.
Regarding their architecture in solar cell applications, there are reported a great variety of selective contacts, from organic to nanostructured films. As hole transport layer, metals of wide work functions are usually employed such as molybdenum or gold. Whereas, for applications in building-integrated photovoltaics, where transparent and flexible back contacts are desired, conductive polymers like $PCPDTBT$ or $PTAA$ are used [69]. For the front contact, normally the ETL, one can use different configurations for the buffer/TCO heterojunction. Since CdS can be deposited via CBD, it is a very attractive option as one can synthesize all the device with only one deposition technique. However, due to its highly toxicity CdS is not the most appropriate selective contact. Thus, layers made of ZnO or TiO_2 are more desirable [70, 71].

Chapter 3

Experimental Part

3.1 Deposition techniques

3.1.1 Thermal (or vacuum) evaporation

Thermal evaporation or vacuum evaporation is a deposition technique included in Physical Vapor Deposition category and, although being one of the oldest techniques, continues to have a widely application in industry and laboratory. It consist on the boiling or sublimation of a small amount of our target material (in powder or wire form) thanks to the drastic heating of the boat containing it. This heating is provided by a high current supply, which will end to thermal energy thanks to Joule effect. Thus, the boat must be made of a high refractory material whose thermal resistance is higher than the one of the target material in order to evaporate only this last one. Once the target's evaporation or sublimation temperature has been reached the vapour will float upwards to the sample' surface where, due to the thermal difference, the material nucleation will start. In order to obtain a good deposition it is necessary to have a High Vacuum ($<2 \cdot 10^{-5} mbar$) pressure inside the working chamber as, otherwise, gaseous contaminants will be embedded in the deposited layer and, because of the particle collisions, the deposition rate and the final layer thickness will be altered. [72, 73]

Figure 3.1: Thermal evaporator equipment. Using a Leybolds Systems, Turbovac TMP 600C and a Alcatel HI2000 for its alimentation.

3.1.2 RF Magnetron Sputtering

Sputtering is a non-thermal PVD process which instead of thermally evaporate the target material, bombards the target with high energetic ions ejecting atoms from it to the sample where the layer is formed by nucleation, obtaining films with high adhesion as we "embed" the material atoms into the samples surface. These energetic ions are generated when an inert gas (normally argon) flux enters to the vacuum chamber when an electrical potential between electrodes (the target and the sample) is alternated at radio frequencies accelerating electrons that collide with the gas atoms and ionize them. If

the collision rate is high enough a condensation of ions is generated and a plasma is obtained. The use of a RF source instead of a DC is in order to avoid the accumulation of charges in some target materials as we are continuously changing the polarity. Also, as we are bombarding the target with ions, secondary electrons will be emitted from it and, in order to contain them, a magnetic field is also applied. That is why we say Magnetron Sputtering. [72, 73]

Figure 3.2: RF Sputtering equipment. Using a Advanced Energy, Cesar RF Power Generation and a Leybolds Systems, UNIVEX 350G glovebox system.

3.1.3 Atomic Layer Deposition (ALD)

Atomic Layer Deposition is one of the most prominent Chemical Vapor Deposition techniques to grow thin layers of a great variety of materials. It has a slow growth rate but it can cover great areas with a high conformal layer and minimizing the below layers damage. That is why, since the early 90s, it gains importance in the semiconductor industry. Its work principle is based on a continuous and sequential introduction of gaseous precursors pulses into a low vacuum chamber where the sample is set. Each precursor pulse will be moved over the samples surface by an inert gas flux and, thanks to the chamber conditions of pressure and temperature, the precursor molecules will interact/react with the surface attaching to it a monoatomic layer of our material. Then repeating these pulses cycles we grow our layer. [72, 74]

Figure 3.3: Atomic Layer Deposition (ALD) equipment. Using Ultratech Savannah ALD System.

3.1.4 Spin-coating

Spin-coating method is a highly simple technique for obtaining planar surfaces and it is widely used in organic (specially polymers) materials deposition. The material is dissolved in a liquid solution that is then dispensed over the sample surface that is spun at high angular speeds, removing part of the solvent and leaving only a thin layer of the material. Finally, an annealing is done to completely remove the remaining solvent. Thus, the thickness of the deposited layer will be controlled and determined by the solution concentration, the angular speed, the viscosity of the dissolution and, also, the surface tension over the sample (if we dissolve in water, the more hydrophilic the sample surface, the thicker will be the deposited layer).[75, 76]

Figure 3.4: Spin coating equipment. Using a Laurell Technologies Corporation, WS-650-23 model.

3.2 Electrical characterisation techniques

3.2.1 Transfer Lenght Method (TLM)

The Transfer Length Method is a widely measurement technique in semiconductor industry as one can extract with a simplified equation and experiment the contact resistivity of a metal-semiconductor interface. The setup consist on measuring the total resistance, via IV test, across two rectangular contacts (WxL) deposited over the semiconductor and separated by a distance d. Thus, the carriers that move from one electrode to the other will notice the resistance of both metal-semiconductor interfaces (or contact resistance, R_c), the resistance of the electrode metal (R_m) and the resistance of the semiconductor "bulk" of length d (R_s): $R_T = 2R_c + 2R_m + Rs$.

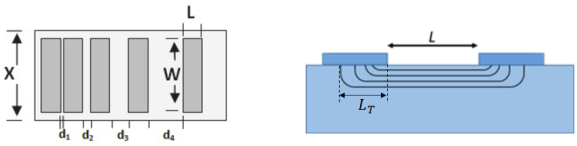

Figure 3.5: Schematic representation of a TLM procedure.

But, considering the metal resistance negligible in front of the semiconductor and contact ones we can simplify it as: $R_T = 2R_c + Rs$. Then, writing the semiconductor resistance in terms of its Sheet Resistance (R_{sh} in $\Omega/\square$), the total resistance is make function of the distance between contacts and by measuring R_T at different pairs of contacts one can make a linear regression and find the R_c at the $d = 0$ axis. Additionally, as the contact resistance is due to the semiconductor sheet just under the metal electrode it can be written as $R_C = R_{sh}L/W$. But, as the current will enter only through a section, "Transfer Length", of the contact (if it is wide enough) the resistance will be $R_C = R_{sh}L_T/W$. Thus, we can extract this length knowing the regression cross with the $R_T = 0$ axis:

$$R_T = R_{sh}\left(2\frac{L_T}{W} + \frac{d}{W}\right)[77]$$

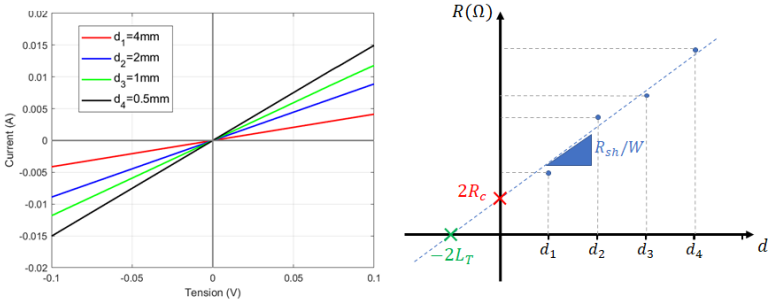

Figure 3.6: IV curves for a TLM series and graphical extraction of contact resistance (R_C) and transfer length (L_T) by TLM method.

3.2.2 Current-Voltage curves

All the TLM measurements, as well as the diodes and solar cells IV measures, have been done employing a four-terminal sensing setup consisting on a pair of terminals that injects current to the device electrodes, while the voltage between contacts is measured with a second pair of terminals. Thus, the parasitic losses in the tension due to wire and finger resistances are avoided. This injected current and the voltage obtained are send from and to a multimeter device that, at the same time, transfers the data recorded to the computer where is processed by a software program [78].

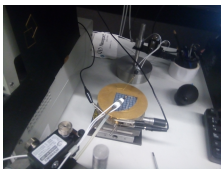

(a)

(b)

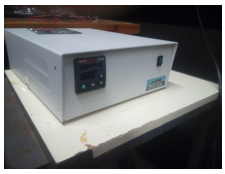

(c)

Figure 3.7: (a) Four-terminal sensing setup, (b) multimeter of measurement Keithley SourceMeter 2601B and, (c) Temperature controller INSTEC STC200.

In the measure of solar cells, a reproducible and controllable illumination conditions (normally 1.5 AM) must be achieved. That is why, the only source of light in the characterization room must be the one belonging to a Solar simulator.

Figure 3.8: Solar simulator NEWPORT 94081A Class ABB Solar Simulator.

3.2.3 Quantum Efficiency

As we have explained in the section of "Solar Cells Parameters" the Quantum efficiency is defined as the ratio between collected electrons and incident photons. In more detail, one can define two Quantum efficiencies, the external and the internal. The first one takes into account all the incident photons reaching the solar cell surface, while the second one only considers those photons that are transmitted to the absorber (it does not enters to reflection studies). The way of measuring this External Quantum efficiency (EQE) is to illuminate (commonly with normal incidence) a defined area of the device surface, making sure that all the light is in the device limits, with a light source that is monochromated and whose intensity is known. Then, we will measure the current obtained (and, thus, the electrons generated) at a specific wavelength for a certain intensity of incident light, EQE(λ). Varying the polarizer, we can sweep different wavelenghts and obtain the window spectrum of our device. It is worthy to mention, that this measurement is done in totally dark conditions and having the light beam pulsed in a specific frequency in order to filter only the photogenerated current coming from our beam and avoid possible interferences.

(a)

(b)

Figure 3.9: (a) PV Measurements QEX10 Quantum Efficiency measurement system and, (b) monochromatic beam illumination over one sample.

3.3 Devices fabrication and experimental results

3.3.1 PEI's TLM over c-Si

As first approach to the incorporation of PEI layer in photovoltaic devices, we carried out a series of Transfer Length Measurements (TLMs) in order to characterise the contact resistivity (and, inderictly, their selectivity) when the PEI is added, first over a c-Si wafer as it is the wideliest theorized and well-known semiconductor. This wafer will be n-type as we suppose (and, afterwards verified) PEI is an ETL, thus as TLM involves a series of contact pairs (or fingers) separated by different distances, we will have a n-n-n structure with "only" a resistive behaviour, i.e. with no non-linearities coming from energetic barriers.
The fabrication process is the following:

1. A silicon wafer (n-type and non-polished backside) is cleaned by a chemical etching consisting in the wafer immersion into a diluted fluorhydric acid (HF) solution, $1(v/v)\%$, during 30s. With this process we suppress all the possible oxides, organic molecules or dust present in the work surface.

2. After the etching, we rapidly deposit the PEI's layer. With a micropipette we take a small volume of the solution containing the polymer (which was stored in a fridge at a constant temperature of $3°C$, and, before doing the deposit, it has been at room temperature for 30 minutes) and we slightly cover the wafer' surface with the solution, only wetting it. Then, with the help of the spin-coating, we set the wafer at $5000rpm$ during $30s$.

3. In order to remove the solvent, the wafer is placed over a hotplate which has been set at the solvent's evaporation temperature. This heating process is carried out only during 30 seconds due to the small thickness of the silicon wafer.

4. Once we have the polymer layer, the metal electrodes are deposited. As we want to extract to a greater extent electrons, the metal used must have a small work function such as aluminium, silver or magnesium. As we will do several depositions and due to the high oxidation rate of magnesium, it is preferable to use aluminium for the depositions. Then, we place into a tungsten boat 4cm of aluminium wire that will be thermally evaporated depositing over the samples' surface a massive electrode (thickness $\in [300, 500]\, nm$) without the need of being extremely precise with the metal thickness as we are not interested in optical properties like transparency. In order to obtain the desired TLM drawing, one must place, before doing the evaporation, a shadow mask over the wafer surface.

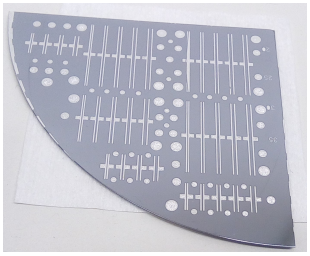

Figure 3.10: Photograph of a silicon wafer quarter with the used TLMs pattern.

At the end we obtain a silicon wafer with the polymeric ETL and several TLMs structures that will give us a statistical database to have the most fairly resistivities and minimizing the possible inconsistencies coming from a nonhomogeneous deposition. And, in order to check the well deposition of the polymeric layer, some optical characterizations are carried out, such as X-ray photoelectron spectroscopy (XPS) or transmission electron microscopy (TEM). With these two techniques, one can obtain the chemical elements and bonds present in the different layers, in addition to their crystallographic planes and thicknesses, from which one can know the interactions happening between layers.

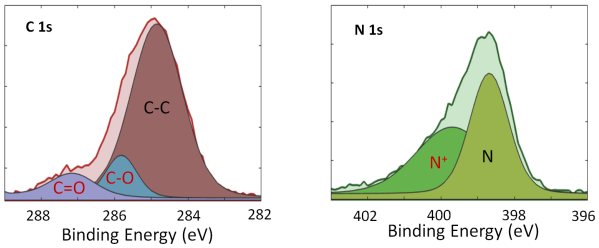

Figure 3.11: XPS spectrum of a TLM sample fabricated by a PEI/EtOH $(0.01(wt)\%)$ dissolution in the energy range of the C 1s and N 1s signals. Source: Eloi Ros Costals

From TEM's data we can confirm the presence of an organic layer between the crystalline silicon and the aluminium electrode with a thickness of approximately 3nm. In this layer we highlight the presence of an oxygen profile (measured by EDS), which may come from the solvent as the PEI does not contain this element. Now, if we focus on the XPS peaks, we find the corresponding bonds of the PEI molecule with its amino groups and carbon chain. However, if we decompose these peaks in their different oxidation states we find contributions which do not have their origin in the polymer, such as single and double carbon-oxygen bonds or the protonated nitrogen.

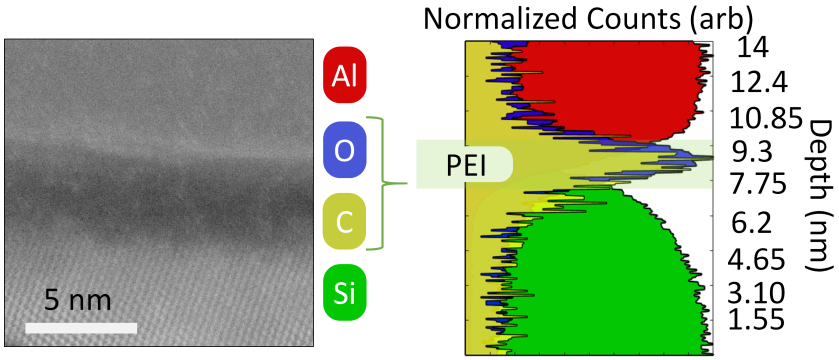

Figure 3.12: TEM image of the transverse section of the ETL stack (c-Si/PEI/Al) and its associated EDS spectrum. Source: Eloi Ros Costals

All these go in accordance with the work principle of amino-based CPs explained in Section 2.4.3, where the interaction of the solvent's hydroxyls with the polymer's

amino groups generates a dipole field. Thus, the Brönstred acid protonates the amino groups of our polymer (which is a Lewis base) and these positive centers will bind to the resulting alkoxide due to its high negative charge density. Thus, we have a dipole formed by the protonated amino group (responsible for the N^+ oxidation state) and the negatively charged oxygen (responsible for the C-O oxidation state), whose interaction/binding will prevent the evaporation of this alkoxide during the annealing step, remaining in the polymeric layer as a counterion.
Additionally, one can design an indirect verification experiment for this theory. As the interaction of the solvent's counterions with the amino group will be partially determined by the solvents molecular dipole moment, one can dissolve the PEI in different solvents, i.e. methanol, ethanol and toluene, and check if the resistivities measured by TLMs vary. This is because the molecular dipole moment of a molecule is a parameter that determines how uniform the charge distribution in a molecule is. Then, a molecule with a non-null dipole moment will have a region with a certain accumulation of positive charge and another with a negative one. In the case of the solvents employed here, the highest molecular dipole will be for methanol, as the oxygen found in its hydroxyl group will act as a negative pole (due to the high electron affinity of the oxygen) which is weakly counteract by the short alkane chain, followed by ethanol (which due to its longer alkane chain the electron affinity of the oxygen is not strong enough to attract the furthest electrons) and, finally, the toluene which its methyl group has a slightly higher electron affinity than the aromatic ring.
Thus, for the solvents with higher molecular dipole moments the interaction with the amino groups of the polymer will be greater and, then, the dipole field generated will be stronger which will lead to a higher transfer of electrons from the electrode to the semiconductor, doping to a greater extent it's interface and, consequently, leading to a lower contact resistivity (Figure 3.13).

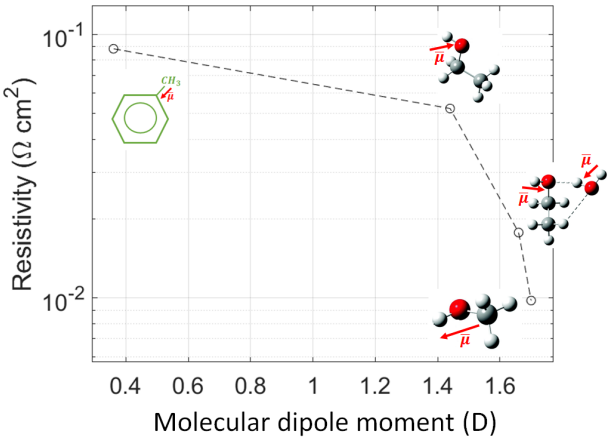

Figure 3.13: Plot showing the variation of the contact resistivity with respect to the solvent's molecular dipole moment. The solutions employed were a $0.01(wt)\%$ of PEI dissolved, respectively, in toluene, ethanol, ethanol+water and methanol

After clarifying the main mechanism behind the ETL behaviour of our PEI layer, the contact optimization must be addressed. For this reason a sweep of concentrations is done in order to find the solution concentration (and thus, the layer thickness) for which the contact resistivity is minimum. Knowing that PEI is electrically insulative, the thickness of the deposited layer must be thin enough to allow the carrier transport from the semiconductor to the electrode by tunneling. Thus, the concentrations under study will be very diluted, i.e. $10^{-3}, 10^{-2}(wt)\%$.

Considering PEI dissolved in ethanol at concentrations of 0.1, 0.05, 0.01, 0.005 and 0.001 $(wt)\%$, and measuring, via TLM, the resistivity of the electron selective contacts comprised of these PEI layers with aluminium electrodes; we find that the optimal concentration, i.e. the lowest resistivity, is found at $0.01(wt)\%$ of PEI/EtOH with a resistivity value of $0.236\Omega \cdot cm^2$.

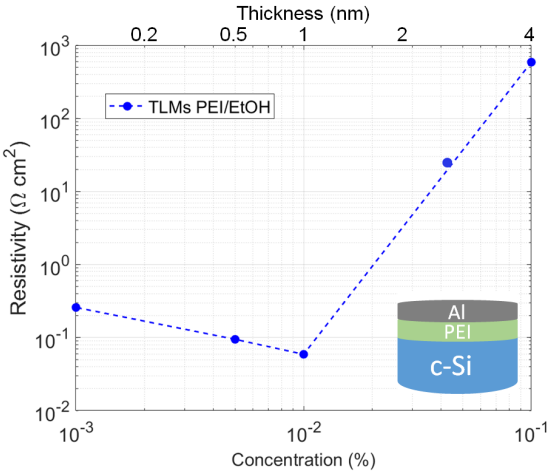

Figure 3.14: Specific contact resistance as a function of PEI concentration.

With this result one can notice that, indeed, the PEI layer has a beneficial effect in the contact because, otherwise, how less amount of the polymer is deposited better contacts should be obtained. But, as we can see, from a certain concentration when we continue reducing the proportion of PEI we increase the contact resistivity. This behaviour, with a "V" shape, can be understood as the combination of two transport mechanisms, one with more presence in small thicknesses of PEI and the other in thicker layers[1]:

- **Thermionic contribution:** When we decrease considerably the amount of polymer between the metal electrode and the semiconductor, this layer is not capable of buffering the direct metal-semiconductor junction. Thus, as the semiconductor starts to see the metal, an energetic barrier associated with the FLP effect competes against the band depletion introduced by the dipolar field. If the thickness of the PEI layer is so thin that the density of amino-counterions dipoles cannot compensate the FLP effect, a net potential barrier will be formed, hindering the transport of electrons. In this case, where a barrier for the electrons is present at the contact interface, the conduction mechanism is described by the Thermionic Emission. In this mechanism, the amount of current extracted from the semiconductor will depend exponentially with the barrier's height:

$$J_{TE} = A^* T^2 \, e^{-\frac{q\Phi_B}{\kappa T}} \left[e^{\frac{qV}{\kappa T}} - 1 \right] \tag{3.1}$$

  where A^* is the Richardson constant.

- **Tunneling contribution:** In the opposite situation, when we have increased in excess the PEI layer thickness, the contact resistivity instead of being impaired due to the presence of an energetic barrier, will grow because of the presence of a dielectric layer hardly surmountable by quantum-tunneling. Then, the transport of electrons will be governed by their tunneling probability across PEI's layer:

$$J_{Tunn} = -qV \int_{-\infty}^{\infty} \mu_n \, n \, \xi \, T(E) \, \frac{\partial E_f}{\partial E} dE \tag{3.2}$$

[1]Model theorized by Eloi Ros Costals (eloi.ros@upc.edu)

with ξ a fitting constant and $T(E) = e^{-2\sqrt{\frac{2m}{\hbar^2(qV_0-E)}}d}$ the tunneling probability for a square potential barrier of width d.

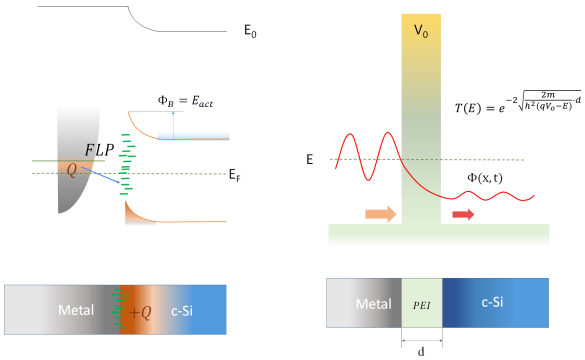

Figure 3.15: Thermionic current due to Fermi Level Pinning emergence for too thin PEI layers (left) and, Tunnelling current for too PEI (right). Source: Eloi Ros Costals

In order to verify this model, one can study the temperature dependence of the resistivity. As for the Thermionic region when increasing the temperature more electrons will have enough thermal energy to overcome the barrier, its resistivity will be proportional to the exponential of the barrier height and also proportional to the exponential of the temperature inverse:

$$\rho_c = \lim_{V\to 0} \frac{\partial J_{TE}}{\partial V} = \frac{k_B}{qA^*T} e^{\frac{\Phi_B}{k_B T}} \tag{3.3}$$

On the other hand, as for the Tunneling region the limiting factor is the width of the polymer layer instead of the barrier height, a slight variation will be found in their resistivities when the measurement temperature is changed.
Thus, if we plot logarithmically the resistivity with respect to $1/k_BT$, we will have that those contacts in the Thermionic region have a linear profile and their slopes being the energetic barrier at the semiconductor interface, while those contacts in the Tunneling regime have a practically constant resistivity (Figure 3.16).

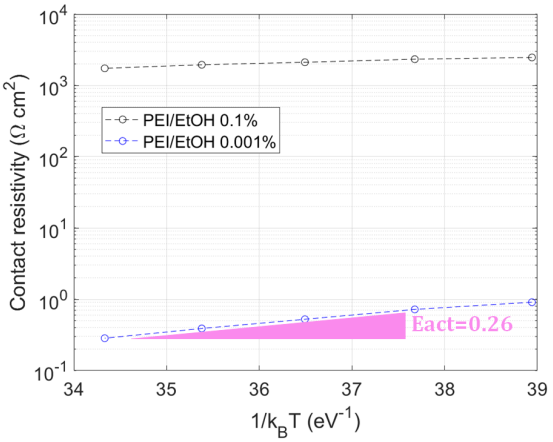

Figure 3.16: Logarithmic plot of the specific contact resistance for two different concentrations as a function of $1/k_BT$.

For the lowest concentration $(0.001(wt.)\%)$ one find a barrier height of $E_{act} = E_c - E_f|_{interface} = 0.26eV$, corroborating the Thermionic Emission transport due to the competence between the FLP and the dipolar effect as there exist an energetic barrier for

electrons but its height is still lower than if we had a direct metal-semiconductor junction, as it would be $E_{act} \sim \frac{2E_g}{3} \sim 0.7eV$ [79].
Regarding the stability and perspective of long-lasting devices implementation of this PEI based contact, the resistivity of the optimal PEI's contact is monitored along a period of three months, under atmospheric conditions.

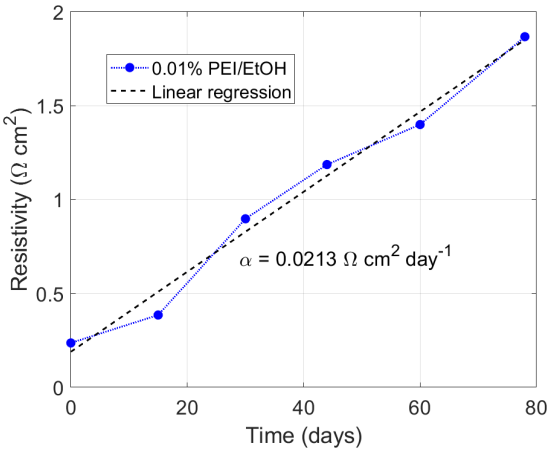

Figure 3.17: Specific contact resistance as a function of time (contact degradation).

From these measurements one should realise that the stability in this selective contact, just as in all organic electronics, is one of the, if not the, most problematic fields. The direct contact with air and the polymer's crystallization and aggregation could be the main responsible of this rapid deterioration, where the contact resistivity has been multiplied by ten in only three months. A way to relieve this deterioration is the device encapsulation in order to isolate the polymer from the atmosphere.

3.3.2 PEI diodes over thin film absorbers

The first approach to PEI application in new absorber materials (proportionated by IREC's team [2]) will be the fabrication and analysis of diode test devices. As the two materials considered, antimony selenide (Sb_2Se_3) and kesterites ($CZTSe$), are intrinsically p-type, we cannot perform the contact characterization technique used in previous works for c-Si (n-type), i.e. the Transfer Length Method (TLM). This is because the TLM performance implies the use of a series of contact pairs, or fingers, separated by different distances. In our case, as the PEI contact acts as an ETL doping with electrons the semiconductor interface thanks to its dipolar field, the TLM structure will behave as an n-p-n structure (i.e. similar to a Bipolar transistor) instead of the desired resistance conduction (n-n-n or p-p-p).
Then, dismissing the TLM characterization, we choose to carry out diode tests that would allow us to compare in a simple way the quality and benefits of our contact. Here, we will study different possible architectures for the electron transport layer (in the case of the HTL we use molybdenum with a slightly selenization) and select the optimum ones for both absorbers. The qualification criteria is the IV curves fitting to a simple diode model with two parasitic resistance (see Figure 2.14).
Thus, the parameters that determine the diode quality are the saturation current density (J_0), the series and shunt resistances (R_s and R_{sh}) and the diode ideality factor (n). With these, a good diode will have an ideality factor as close as possible to 1, a series resistance and a saturation current density as small as possible ($R_s \sim 1\Omega, J_0 \sim 10^{-9} A/cm^2$) and a shunt resistance as big as possible ($R_{sh} \sim 10^6\Omega$).

[2] Alex Jiménez (ajimenez@irec.cat) & Maykel Jiménez (maykel.jimenez@upc.edu)

At the end, the goal of all this study is to fabricate solar cells based on kesterites and antimony selenide absorbers with our dipolar contact in substitution (or enhancing) of the typical used CdS front contact due to the toxicity issues associated with cadmium. Thus, different alternative architectures involving our polymer will be tested in order to find the most promising one.

Antimony Selenide diodes

For this absorber the typical electron transport layer consists of a CdS layer, with the incorporation in some literature of an intermedium passivation layer between this and the absorber, i.e. TiO_2 [80]. In our study, we decided to try first the PEI polymer directly contacted over the antimony selenide in order to distinguish if the architecture employed in c-Si also works. Thus, we deposit different widths of PEI over the absorber as an attempt of finding the optimum concentration, i.e. the one giving the smallest serial resistance in the diode model similarly to the V model found for $c-Si$. Thus, similarly to the procedure followed in the TLM experiments, we deposit the dissolution of PEI with ethanol through spin-coating directly over the Sb_2Se_3 layer and, a thermal annealing at $80°C$ during $6min$ (longer time due to the glass substrate that have these samples) is done in order to evaporate the solvent. In this absorber we do not treat the surface with a chemical etching as this process is still under study. Finally, the aluminium contacts (with an area of $0.1cm^2$) are deposited via thermal evaporation.

(a) (b)

Figure 3.18: (a) Sb_2Se_3 diode sample and, (b) drawing of its architecture.

As initially we have no previous knowledge of how the polymer will interact with this new absorber, a wide sweep of concentrations is done: $[PEI/EtOH] = 1$, 0.1, 0.01 and $0.001(wt)\%$. And, the resulting IV curve are fitted to the diode model (Figure 3.19).

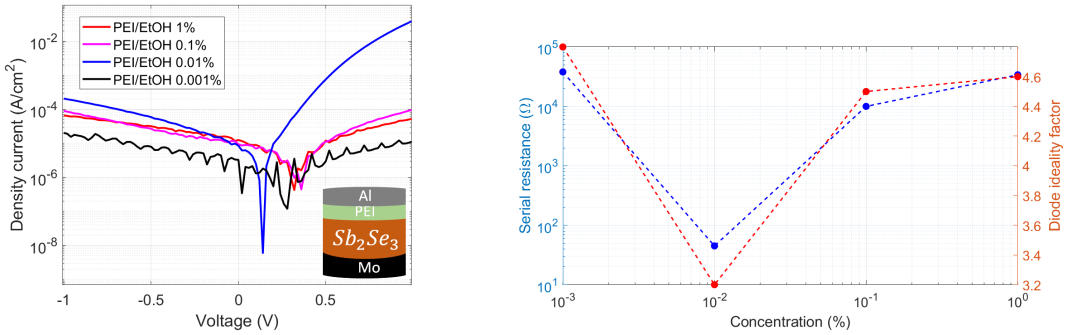

(a) (b)

Figure 3.19: (a) I-V curves of Sb_2Se_3 diodes for different PEI thicknesses and, (b) fitted ideality factors and series resistance as a function of PEI concentration.

From this, one can note that no diode behaviour is appreciable for all the samples (ideality factors $n > 3$), resembling to a Schottky barrier where the current is due to the diffusion of the majority carriers, holes in this case, instead of the desired minority

current. However, a clearly improvement is obtained for the PEI layer coming from the solution of 0.01% ($R_s = 45.2\Omega$, $R_{sh} = 100k\Omega$, $n = 3.2$), having for the direct mode a more important injection in comparison with the inverse mode. And, analysing the diode parameters as a function of PEI's concentration (i.e. thickness) we recover the "V" shape found for PEI contact's resistivity over c-Si. Thus, one can suppose that the model explained for c-Si/PEI contact also applies over this absorber and, that the contact resistance of the ETL dominates over the other series resistance contribution (semiconductor and back contact resistances) as its behaviour is not shadowed.

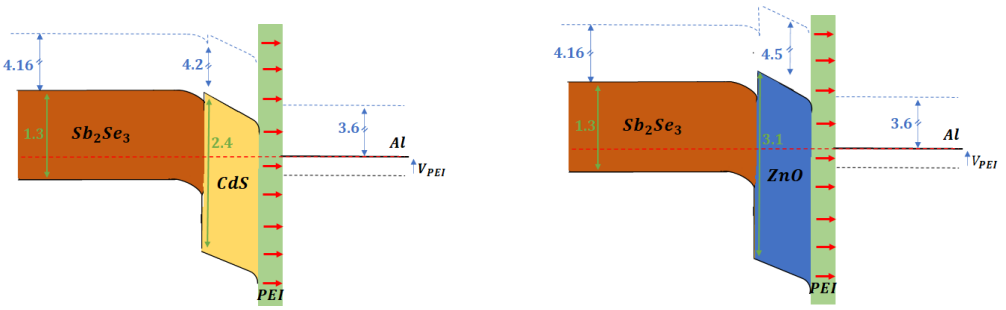

(a) (b)

Figure 3.20: Band alignment of the buffer/PEI based ETLs over Sb_2Se_3: (a) Standard CdS and, (b) $i-ZnO$.

Then, as the direct PEI deposition over the absorber seems to be not enough to stop the transport of holes across the contact, the next step is to incorporate a wide band gap layer as buffer between the absorber and the contact in order to have a huge barrier for holes. Thus, a p-i-n junction will be obtained.
Firstly, the widespread buffer layer of CdS is considered in order to have an idea of the PEI effect in the typical structure for this absorber. Regarding the fabrication process and the physical properties of this CdS, we have deposit around 60nm by chemical bath deposition [62] and we consider a band gap and an electronic affinity of 2.4 and 4.2 eV, respectively. Again, as we will deposit the polymer over a new semiconductor, we decided to do a sweep of PEI widths. Concretely, and expecting that with the CdS coating the surfaces roughness will decrease, we only study the three concentrations of 0.1%, 0.01% and 0.001%, disregarding the solution of 1% analysed for the first diodes.

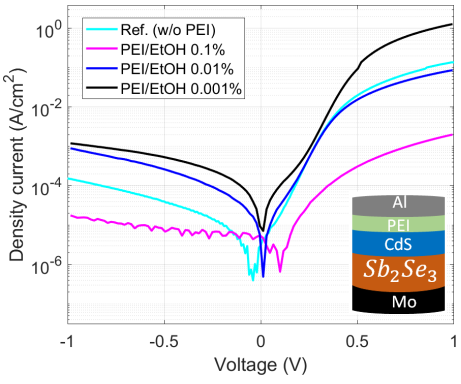

Figure 3.21: I-V curves of Sb_2Se_3/CdS diodes for different PEI concentrations.

	n	$R_s(\Omega)$
Ref. (w/o PEI)	1.65	41.4
PEI/EtOH 0.001%	1.51	3.4
PEI/EtOH 0.01%	1.59	61
PEI/EtOH 0.1%	3.7	1900

Table 3.1: Table with the ideality factors and series resistance of Sb_2Se_3/CdS diodes for different of PEI concentrations.

From the results showed in Figure 3.21 and Table 3.1, we can state that a clear improvement is found with respect to the Sb_2Se_3/PEI samples having a clear diode behaviour

and that thinner layers of PEI give better outputs, as we expected due to the well-known ETL behaviour of CdS. But not only this, we find that with the incorporation of PEI the device performance is improved having its optimum at the lowest concentration of PEI, 0.001%, where high asymmetry between direct and inverse modes is obtained leading to an ideallity factor of 1.51. Thus, the dipolar field generated by the PEI layer depletes the buffer bands facilitating the quantum tunneling of electrons across the conduction band. Also, an interesting result is that the buffer layer shifts the optimum concentration to lower values, having a "V" shape in the R_s shifted to the left when superposing it with the one obtained for the samples without CdS.
However, due to the inherent toxicity issues and the unsatisfactory stability of CdS, an alternative buffer layer involving i-ZnO [81, 70, 80] is here studied. In this case, as we have the experience of the CdS buffer layer, we deposit directly the optimal PEI concentration of 0.001% over the zinc oxide layer. In the study we also compare two different oxide deposition methods for the ZnO, RF sputtering and ALD, but always mantaining the layer thickness (50nm).
If we consider that the ZnO has a band gap of 3.1 eV [82] and an electron affinity of 4.5 eV [83] both barriers, for electrons and holes, are increased when compared with the CdS due to the bigger band gap and differences between conduction and valance bands. However, the barrier present for holes will be higher than the one for electrons and the application of PEI that depletes the band will facilitate the tunneling through the conduction band for the electrons while the barrier for the holes is increased even more. Thus, we expect to see an improvement when the PEI is introduced.

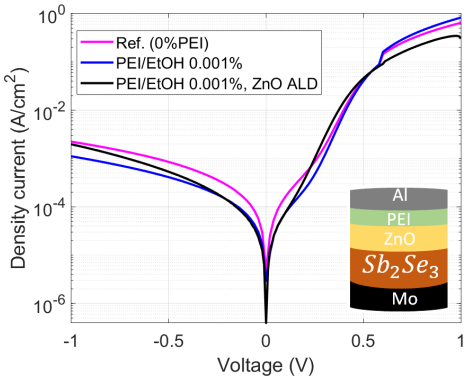

Figure 3.22: I-V curves of Sb_2Se_3/ZnO diodes for different PEI concentrations.

	n	$R_s(\Omega)$
Ref. (w/o PEI)	1.7	6.5
PEI/EtOH 0.001%	1.65	4.85
PEI/EtOH 0.001% (ALD)	1.7	12.9

Table 3.2: Table with the ideality factors and series resistance of Sb_2Se_3/ZnO diodes for different of PEI concentrations.

Effectively, the PEI layer improves the diode behaviour of the ZnO and, when the different deposition techniques are compared, one can notice that, although obtaining the same order of magnitudes, the buffer layer coming from sputtering has a better performance than the one deposited by ALD. A possible explanation could be that with the sputtering deposition we obtain a higher density of oxygen vacants and, thus, we have a more n-type semiconductor instead of intrinsic [84].
Interestingly, with these last results we have obtained a CdS-free structure that can compete with the typicl CdS buffer layer but being non-toxic and earth-abundant.
Comparing the contact consisting of ZnO/PEI with the CdS reference we see how the diode ideality factor is the same but having an important improvement with the series resistance. Regarding the shunts differences, it can be attributed to inhomogeneities in the absorber samples due to its strongly sensitivity to fabrication conditions, being a recurrent issue the appeareance of pin-holes.

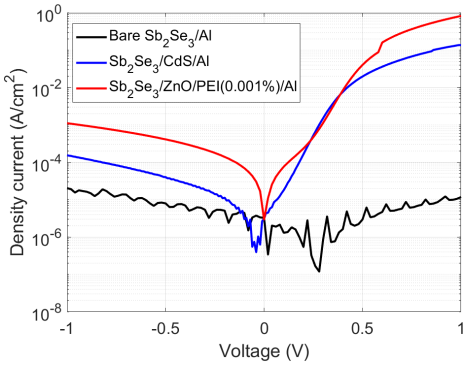

Figure 3.23: I-V curves comparison between the diodes with the standard CdS structure and our ZnO/PEI alternative.

	n	$R_s(\Omega)$	$R_{sh}(k\Omega)$
Al	–	–	–
CdS/Al	1.65	41.4	158
ZnO/PEI/Al	1.65	4.85	12.5

Table 3.3: Comparison table with the fitting parameters for different Sb_2Se_3 front contacts.

Thus, the ZnO/PEI seems to be a promising candidate for a CdS-free antimony selenide solar cell.

Kesterite diodes

In this second section we will perform the same analysis as above but with another thin-film absorber, CZTSe. This material, as we have already explained in the Theoretical Background, has arisen in recent years as a promising absorber for thin-film solar cells with a lower environmental footprint and a more reachable industrial production thanks to its alloying components. Here, the samples studied have been synthesised using IREC's germanium recipes, i.e. setting two Ge layers of 5nm and 10nm over and below the sputtered metallic composite [59]. Again, the most common ETL used in this kind of solar cells is a CdS layer. Thus, we will analyse the effect of PEI over three different architectures: over the kesterite itself, over the typical contact of CZTSe and CdS and, as an alternative attempt for this last one, over the heterojunction composed of CZTSe and TiO_2.

The procedure followed to prepare the samples is the same used for the antimony selenide series, but with the difference of the chemical etching. As the most limiting factors in the efficiency of kesterite' solar cells are the formation of secondary phases, oxides and pin-holes in the material, we try to mitigate the second by treating it with a chemical bath. First, following the IREC's recipe [60], we submit the kesterite to an oxidizing chemical etching in acidic $KMnO_4$ solution (40 s) followed by a $(NH_4)_2S$ immersion (2 min) and a 2 min etching in a 2% KCN aqueous solution. Additionally, before depositing the next layers, we do a final etching by immersing the kesterites in a HF/H_2O $1(v/v)\%$ solution for 20s, which has been reported in the group to improve the cell's performance.

Once the absorber has been cleaned of oxides, we deposit the layers forming the different ETLs; either the direct PEI deposition via spin-coating, the CdS growth by chemical bath deposition or the TiO_2 deposition through ALD [3], followed, all them, by the Al contacts evaporation to finish the diode devices.

The first diode analysis done with this absorber is the seek out of the optimum PEI solution directly deposited over the kesterite. In a similar way to the study performed

[3]Precursors (75°C): $H_2O + TDMAT$, chamber pressure of 0.42mbar, deposition temperature of 100°C and one cycle consists on pulses of 0.8s and 0.05s for $TDMAT$ and H_2O, with a growth rate of 1Å/cycle.

for antimony selenide, we select four different concentrations distant one from each other (1%, 0.1%, 0.01% and 0.001%) in order to cover the widest range as we do not have previous information of how our polymer will affect this new semiconductor.

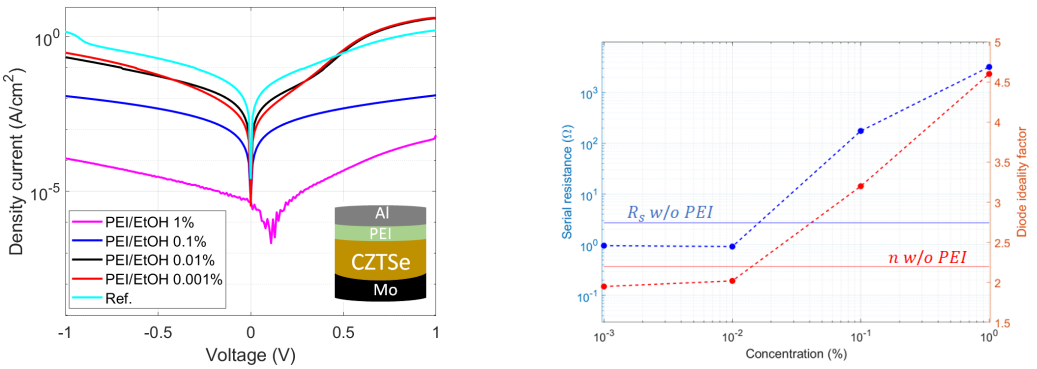

(a) (b)

Figure 3.24: (a) I-V curves of $CZTSe$ diodes for different PEI widths and, (b) fitted ideality factors and series resistance as a function of PEI concentration.

Looking first at the reference sample (Figure 3.24a), i.e. without PEI layer, we see clearly the expected ohmic behaviour as we have only deposited an Al contact over a p-type semiconductor. When we deposit the PEI we wish to obtain a diode behaviour. However, a very symmetric curve is obtained instead. The high density population of pin-holes present in kesterites causes the device's short-circuit between the front and back contacts when the Al layer is deposited. But comparing with the reference sample, one can note that a major rectification is done by the polymer layer obtained from a solution with a concentration between 0.01% and 0.001% as are the samples with most asymmetric curves, and with a more pronounced diode behaviour ($n = 2.02\,\&\,1.95$ and $R_s = 0.92\,\&\,0.96\Omega$, respectively, compared with 2.2 and 2.7Ω of the reference). If we increase the polymer layer's thickness we lose most of the improvements achieved in the diode and, also, we hinder the current transmission.

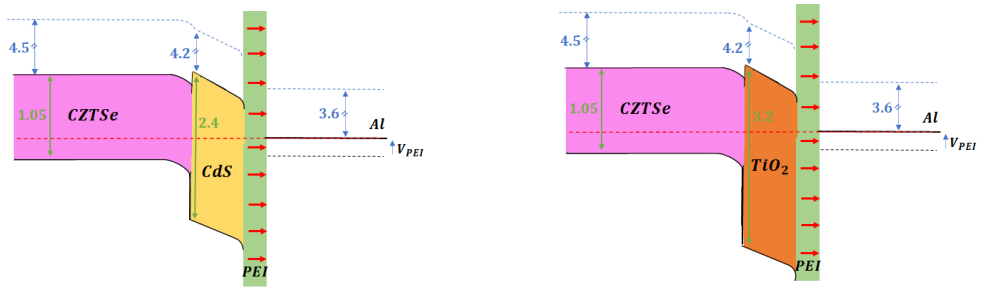

(a) (b)

Figure 3.25: Band alignment of the buffer/PEI based ETLs over $CZTSe$: (a) Standard CdS and, (b) TiO_2.

After having studied the direct contact of PEI with kesterites we will analyse the bi-layer structures of CdS/PEI and TiO_2/PEI. In the first case, as we have the previous information obtained during the antimony selenide tests, we suppose that the optimum concentration is at low PEI densities. For this reason we consider three samples of $CZTSe/CdS$ over which we deposit the PEI solutions of 0.005% and 0.001% and leaving a remaining one as reference.

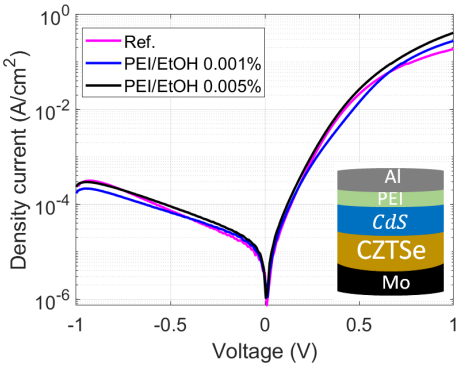

Figure 3.26: I-V curves of $CZTSe/CdS$ diodes for different PEI concentrations.

	n	$R_s(\Omega)$
Ref. (w/o PEI)	2.45	21.6
PEI/EtOH 0.001%	2.68	11.7
PEI/EtOH 0.005%	2.56	8.4

Table 3.4: Table with the ideality factors and series resistance of $CZTSe/CdS$ diodes for different of PEI concentrations.

The results obtained show a slight improvement of the diode output when the PEI layer is incorporated, specially in respect of the series resistance. Interestingly, in contrast to the $Sb_2Se_3/CdS/PEI$, the more polymer the better the device come out. Although having initially a higher ideality factor when the thinnest PEI layer is deposited compared with the reference one, when we double the dissolution's concentration an important improvement is achieved in n's value. Then, in the next devices (solar cells) higher concentrations will be employed.
As an alternative to the CdS buffer layer, we implement a TiO_2 layer deposited by ALD which due to its wider band gap and n-type behaviour [85] seems to be a good candidate for this absorber, specially thanks to the high energetic barrier that will have for holes [86]. However, due to its low conductivity, thin widths must be taken in order to allow the transport by tunneling.
In this first approach we deposit 2nm of TiO_2 as it is the optimal thickness found for ETL over silicon [85]. And, over one sample, a PEI layer is also introduced in order to know its effect and try to reach a diode behaviour similar to the one obtained with the CdS.

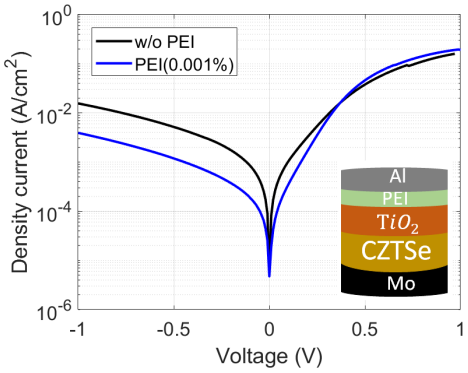

Figure 3.27: I-V curves of $CZTSe/TiO_2$ diodes for different PEI concentrations.

	n	$R_s(\Omega)$	$R_{sh}(k\Omega)$
Ref. (w/o PEI)	2.34	31.5	1.05
PEI/EtOH 0.001%	2.26	24.3	6

Table 3.5: Table with the ideality factors and series resistance of $CZTSe/TiO_2$ diodes for different of PEI concentrations.

With these results, regarding the TiO_2 buffer layer, one can extract two important facts. First, that the TiO_2 does not select electrons in an enough preferential form as the current in the inverse polarization grows in a considerable way. This low shunt resistance

can be attributed to the use of a too thin layer as the thickness employed was the optimal for c-Si, which has a very smoth surface whereas kesterites are characterized by a great roughness ($\sim 100nm$) leading to a possible non-conformal coating. Thus, in the next devices (solar cells) a thicker layer of TiO_2 will be employed but always being thin enough to allow tunneling. Second, that the introduction of PEI layer over the TiO_2 improves all the diode parameters, highlighting the increase in the shunt resistance.

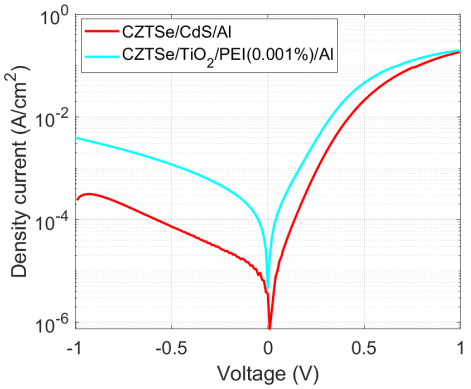

Figure 3.28: Comparison between the diodes with standard CdS structure and our TiO_2/PEI.

	n	$R_s(\Omega)$	$R_{sh}(k\Omega)$
CdS/Al	2.45	21.6	182.5
TiO_2/PEI/Al	2.26	24.3	6

Table 3.6: Table with the fitting parameters for different Sb_2Se_3 front contacts.

If we compare this CdS-free structure involving TiO_2 and PEI with the reference CdS diode, we see that a quite similar diode is obtained in the direct mode, even having a better diode ideality factor for the TiO_2 structure. With this, one might think that if we are capable of reducing the shunt troubles in the CdS-free structure, either via the use of thicker TiO_2 or PEI layers, this could be a promising alternative to the common sulphide based contact in kesterite solar cells.

3.3.3 Thin film solar cells with PEI as electron transport layer

In this final section we try to implement the knowledge acquired along the past experimental sections in order to fabricate thin-film photovoltaic devices with this organic selective contact. The most important difference with the diode tests is that here a window layer must be deposited instead of the aluminium electrode. This, as we will see, will lead to several technical challenges related with the damage of underneath layers and with the decrease in the PEI effect strength.

Antimony Selenide solar cells

As first photovoltaic device we depart from the promising results obtained in the diode tests, where a very similar performance was achieved replacing CdS by i-ZnO. Regarding the window layer, as we will employ a i-ZnO buffer, we decided to implement a bilayer stack by depositing over the buffer zinc oxide doped with aluminium, ZnO:Al or AZO, which can provide a high transparency front contact [87, 88]. Also, the favourable use of AZO instead of other TCO, such as indium-tin-oxide (ITO), is supported (although it is less conductive) by its widely application in industry and the possibility of depositing it via Atomic Layer Deposition, which will be a low damaging process for the organic layer, can provide a highly versatile and tunable electrical properties for the deposited layer [89] and, thanks to its soft deposition, short-circuits problems derived from metallic ions diffusion across the absorber will be avoid.

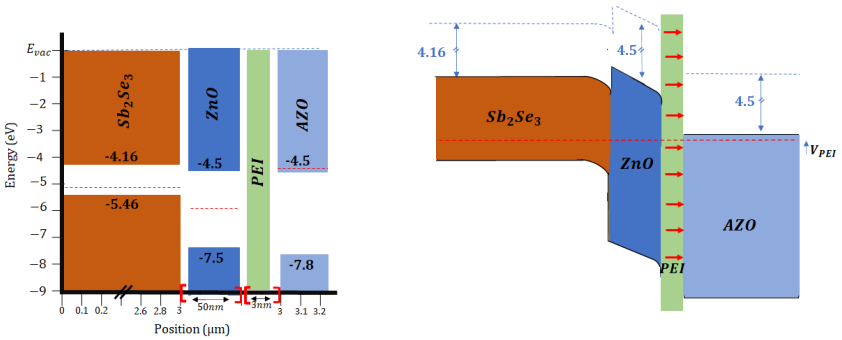

Figure 3.29: $Sb_2Se_3/ZnO/PEI/AZO$ stack layers disposition with electrical features and band alignment of the stack under equilibrium.

Then, the experimental procedure consists on:

- Deposite the i-ZnO buffer layer over the Mo/Sb_2Se_3 samples provided by IREC's team. This i-ZnO will be layerd by ALD (even the better performance by sputtering deposition found in the diode test) in order to use the same equipment along all the process fabrication steps, simplifying in a considerable way the device assembly. The films were deposited using the ALD system shown in Section 3.1.3 at a deposition temperature of $130°C$ and a working pressure of 0.38mbar. Diethylzinc (DEZ, UP chemical Co., Ltd., Korea) was used as precursors for the deposition of ZnO and water vapor was used as a reactant. The precursor and the reactant were contained in a cylinder held at $75°C$ and room temperature, respectively. DEZ was delivered into a chamber with an N_2 carrier flow of 20 sccm and one ALD cycle consisted of water vapor pulsing (0.02 s), N_2 purge (5 s), DEZ pulsing (0.015 s), and N_2 purge (5 s). This cycle was repeated for a total of 300 times, obtaining a film of thickness ranged from 50 to 54nm and an approximately sheet resistance of $R_{sheet} \approx 35k\Omega/\square$.

- Then, the PEI layer is deposited via spin-coatting following the same conditions as in the diode tests. We slightly cover the wafer' surface with the PEI/EtOH solution, only wetting it and, we set the wafer at $5000rpm$ during $30s$. Then, the solvent is removed by a thermal treatment at $80°C$ during 6min, using a Selecta Rectangular precision hotplate Plactronic 6157100.

- Following the PEI incorporation, the AZO window layer is deposited using the same ALD system, at a deposition temperature of $150°C$ and a working pressure of 0.4mbar. The same precursor was used for the ZnO while trimethylaluminum (TMA, UP chemical Co., Ltd., Korea) were used as precursor for Al_2O_3. Water vapor was used as a reactant. The ZnO precursor and the reactant were contained in the same conditions as in the i-ZnO deposition and the Al_2O_3 precursors was held at room temperature. DEZ was delivered into a chamber with an N_2 carrier flow of 20 sccm and one ALD cycle consisted of DEZ/TMA pulsing (0.015/0.05 s), N_2 purge (5 s), water vapor pulsing (0.02 s), and N_2 purge (5 s). For the deposition of AZO films, 19 ZnO ALD cycles and one Al_2O_3 ALD cycle were repeatedly deposited for total 45 ALD cycles $((19+1)45)$. With this deposition we obtained a film of thickness and sheet resistance ranged from 138 to 146nm and 184 to $230\Omega/\square$.

- Finally, we thermally evaporate (using the system shown in Section 3.1.1) small silver dots at each device in order to improve and facilitate the contact during

the characterization processes. The silver pellets of 99.99% purity are evaporated into a tungsten boat when the chamber pressure is lower than $3 \cdot 10^{-5}$mbar and the current supplied to the boat is higher than 270A.

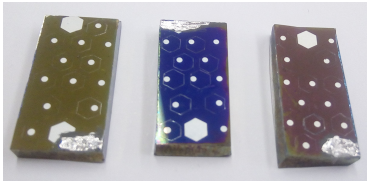

Figure 3.30: From left to right: $Mo/Sb_2Se_3/PEI/AZO$, $Mo/Sb_2Se_3/ZnO(50nm)/PEI/AZO$ and, $Mo/Sb_2Se_3/ZnO(20nm)/PEI/AZO$ solar cells.

Similarly to the diode tests, we try different concentrations of PEI in order to notice a possible optimal thickness. In the diode, we found that the optimal PEI layer was the one whose concentration was minimum, $0.001(wt)\%$. However, as we have changed the electrode over the polymer by a less conductive material, one may expect a shift to higher concentrations in order to have the same dipolar strength.
In this study, we prepared four samples, one as reference (without PEI) and three samples with PEI layers coming from solutions of $0.001(wt)\%$, $0.005(wt)\%$ and, $0.01(wt)\%$ in ethanol.

	$w/o\ PEI$	$PEI\ 0.001\%$	$PEI\ 0.005\%$	$PEI\ 0.01\%$
$V_{oc}(mV)$	240	290	290	340
$J_{sc}(mA/cm^2)$	19.35	21.05	16.91	20.67
$FF(\%)$	33.07	31.39	35.36	34.42
$\mu(\%)$	1.536	1.917	1.734	2.411

Table 3.7: $Mo/Sb_2Se_3/ZnO/PEI/AZO$ solar cell parameters for different PEI concentrations.

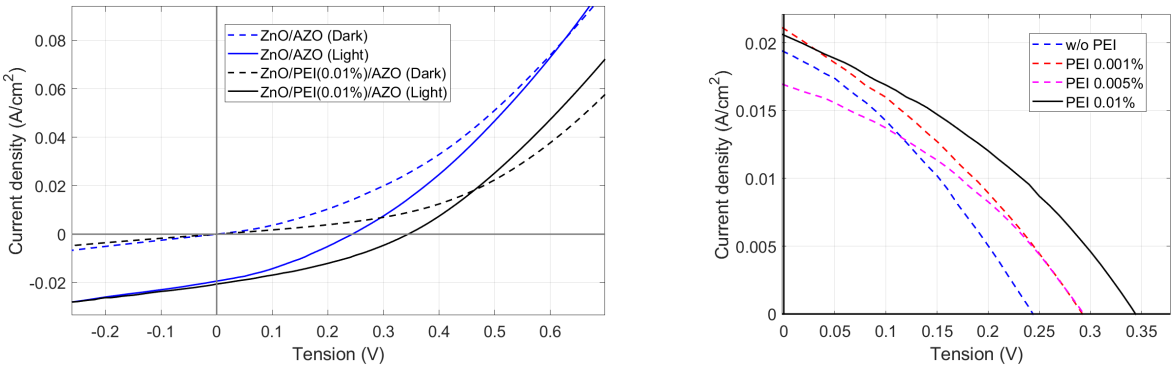

(a) (b)

Figure 3.31: Cells I-V with different PEI concentrations: (a) Comparison between reference ($Sb_2Se_3/ZnO/AZO$) and 0.01% PEI samples, and (b) first quadrant amplification.

From Table 3.7, we can notice a heavily improvement in the open-circuit voltage when the PEI layer is incorporated as well as in the Fill-Factor. Thus, one can see how the PEI enhances the selectivity of our front contact, and that how higher is the PEI concentration (equivalent to layer thickness) better is the solar cell performance, what agrees with the above-mentioned electrode change. Comparing the reference sample

(w/o PEI) with the one with 0.01% of PEI, a drastic improvement is obtained. From the 240mV open-circuit voltage of the reference to the 340mV of the highest concentration, we have increased in 100mV the maximum voltage that the device is able to give, a growth of more than 40%. This, added to the slightly improvement in the FF and J_{sc}, leads to a maximum efficiency of the 2.411% for a CdS-free Antimony Selenide solar cell, being a highly promising result.
However, if we look to the IV curves at the inverse polarization there exist important shunt leaks that can be responsible of the FF values under 40%.
Nevertheless, this low FF, also, could be attributable to the high series resistance that carries our buffer layer. In order to distinguish the origin of this low FF, we prepare a sample without the buffer layer and we compare it with the best device obtained before.

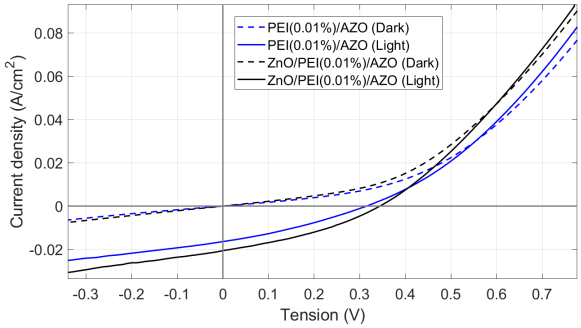

Figure 3.32: Effect of ZnO buffer layer in the cell performance.

	w/o buffer	With buffer
$V_{oc}(mV)$	320	340
$J_{sc}(mA/cm^2)$	18.85	20.67
$FF(\%)$	30.19	34.42
$\mu(\%)$	1.584	2.411

Table 3.8: Solar cell parameters comparison between $Sb_2Se_3/PEI(0.01\%)/AZO$ and $Sb_2Se_3/ZnO/PEI(0.01\%)/AZO$ devices.

With this experiment one can see how the buffer layer instead of being detrimental for the series resistance, seems to effect similarly, or even better, to the case of no involving a buffer layer as the IV slope in large positive tensions remains practically unaltered. And, the same think happens with the shunts. Thus, the low values in the FF seems to be responsibility of shunt leaks that, in their turn, are due to defects like pin-holes in the absorber as they are independent of the contact stack. However, the most important conclusion that one may extract from these results is that the buffer layer is necessary to obtain a better solar cell performance as the resultant p-i-n junction seems to select to a better extent the electrons as we lose less voltage in interface recombinations (the V_{oc} is higher when the i-ZnO is included).

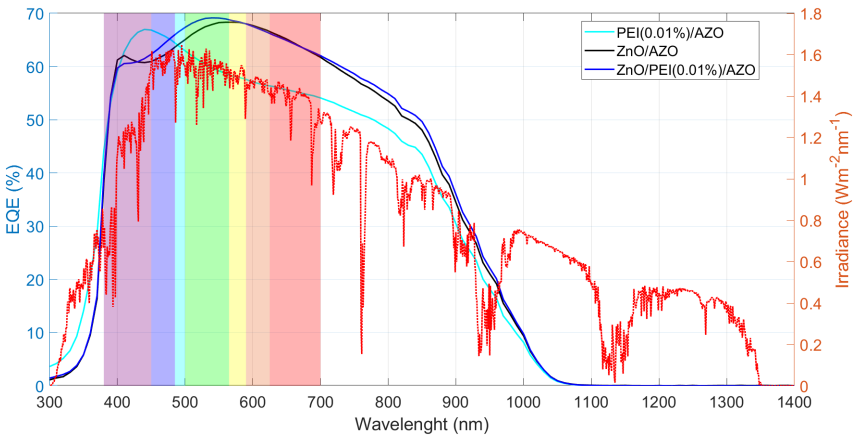

Figure 3.33: External Quantum efficiencies of the three main strucutres: $Sb_2Se_3/ZnO/AZO$, $Sb_2Se_3/ZnO/PEI(0.01\%)/AZO$ and, $Sb_2Se_3/PEI(0.01\%)/AZO$.

In addition, one can measure the Quantum Efficiency in order to know the effect of, both, PEI and buffer layer in the absorbance spectrum. Firstly, we can see that the buffer layer has a very important role in the antireflective quality of the window stack, as the samples incorporating it has a flater spectrum, absorbing to a greater extent the visible range. The EQEs does not drop under the 60% until reaching wavelengths over 700 nm while in the sample without buffer layer drops to EQEs under the 60% at a wavelength close to 550nm. And, secondly, the effect of PEI consist on shifting to lower wavelengths the absorbance maximum, probably due to an optical question instead of an electrical one, as we have inserted a thin plastic layer. Thus, a greater photogenerated current will be obtained for the i-ZnO/PEI sample, as we have already seen.
Also, with these EQEs (assuming an homogeneous absorber) one can extract the band gap of our antimony selenide: E_g=1.305 $\pm$ 0.012eV, what agrees with literature [64, 90].

Kesterite solar cells

In this thin-film absorber we change the employed TCO by Indium-tin-oxide (ITO) as it is the one with more presence in literature and it has a higher conductivity with respect to AZO. However, as we will deposit it through Sputtering, some difficulties can emerge due to its harsh character. First of all, if we try to deposit directly the ITO over the PEI based ETL, the stack below, independently of the buffer layer used, will be not enough to avoid the diffusion of In ions which will reach the back contact thanks to kesterite's high density of pin-holes and the device will short-circuit (Figure 3.34 (a)).
Another difficulty that we obtain by sputtering deposition is the damage over our polymeric layer derived from the plasma exposition. The UV photons that will be generated and the high-energetic collisions of target atoms and clusters can, respectively, break the polymeric chain bonds and erode the organic layer leading to the polymer degradation and to uncovered regions (non-conformal PEI layer). This can be appreciated in Figure 3.34 (b), where the same $Mo/MoSe_2/CZTSe/TiO_2/PEI/Mg$ diode is fabricated only changing the deposition technique for the magnesium. As we can see, the two diodes appear to be the same but one displaced to higher currents. The slopes at direct and inverse modes are practically the same. The series and shunt resistance are low altered by the different electrode deposition techniques (the magnesium quality seems to be the same for both techniques). However, as the current obtained for the evaporated Mg diode is one order of magnitude bigger than the one obtained through sputtering, one may justify it as the PEI degradation under plasma exposition that has leaded to a lower carrier selectivity and, thus, to a lower collection of current.

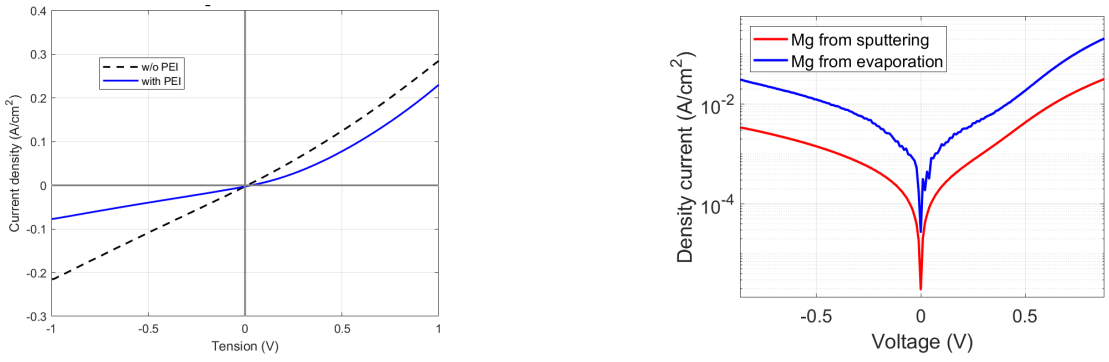

(a) (b)

Figure 3.34: (a) Light IV curves for $Mo/MoSe_2/CZTSe/TiO_2(4nm)/PEI/ITO$ cells and, (b) Comparison between deposition techniques over PEI: IV curves for $Mo(Se)/CZTSe/TiO_2(4nm)/PEI/Mg$ diodes with sputtered and evaporated Mg.

Then, in order to prevent the In diffusion and to protect the polymeric layer, we introduce an intrinsic layer of ZnO by ALD before the ITO sputtering. Therefore, as it has a low conductivity, if some of its atoms diffuse until the back contact no short-circuit will emerge and it will be thick enough to buffer the plasma with respect the organic layer.
After this correction, and seeing that diodes and cells obtained in the previous tests (Figure 3.34), where TiO_2 has been used, have a shy performance, we will try the standrad CdS cell architecture first in order to assure the obtention of a good device since the beginning and to show that with the PEI incorporation one can enhance it.

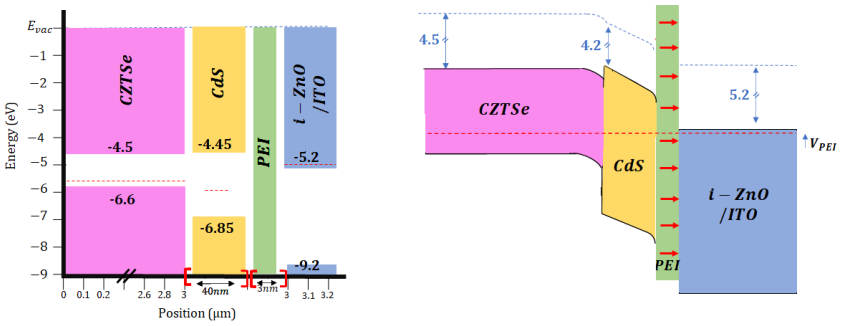

Figure 3.35: $CZTSe/CdS/PEI/i-ZnO/ITO$ stack layers disposition with electrical features and band alignment of the stack under equilibrium.

Thus, the fabrication steps (starting from the $Mo/CZTSe/CdS$ samples provided by IREC's team) will be:

- PEI layer deposition via spin-coatting is performed following the same conditions as in the previous experiments. We slightly cover the wafer' surface with the PEI/EtOH solution, only wetting it and, we set the wafer at $5000rpm$ during $30s$. Then, the solvent is removed by a thermal treatment at $80°C$ during 6min.

- Then, the i-ZnO protecting layer is deposited by ALD in order to be the softest as possible over the polymer layer. The films were deposited using exactly the same ALD system and cycles, reaching again thicknesses ranged from 50 to 54nm and an approximately sheet resistance of $R_{sheet} \approx 35k\Omega/sq$.

- Following the protecting layer deposition, the ITO window layer is deposited via RF Magnetron Sputtering at room temperature and using the equipement seen in Section 3.1.2. The Ar process pressure is set at $1.3 \cdot 10^{-3}$mbar and the power transmited to the plasma is fixed at 50W. With this working conditions we do a 100min duration deposition process, obtaining a film of thickness ranged from 140 to 150nm and an approximately sheet resistance of $R_{sheet} \approx 250\Omega/\square$.

- Finally, we thermally evaporate small silver dots at each device in order to improve and facilitate the contact during the characterization processes.

Again, starting from the results obtained during the diode tests, we study PEI concentrations around the optimal of 0.001% found for CdS buffer layer diodes. Comparing the cell parameters obtained for a reference sample without PEI with two samples involving PEI layers coming from solutions in ethanol of 0.001% and 0.005%, we clearly obtain that only with a thin film of our polymer the device performnce is drastically improved, increasing its open-circuit voltatge in 50mV (a passivation effect is obtained), and that the solar cell parameters are improved with the increase of PEI concentration, what agrees with the change in the electrode.

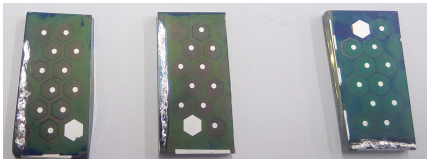

Figure 3.36: From left to right: Mo/CZTSe/CdS/i-ZnO/ITO, Mo/CZTSe/CdS/ /PEI(0.001%)/i-ZnO/ITO and, Mo/CZTSe/CdS/PEI(0.005%)/i-ZnO/ITO solar cells.

	$w/o\ PEI$	$PEI\ 0.001\%$	$PEI\ 0.005\%$
$V_{oc}(mV)$	280	330	330
$J_{sc}(mA/cm^2)$	18.35	21.04	25.33
$FF(\%)$	31.52	36.33	36.69
$\mu(\%)$	1.621	2.522	3.066

Table 3.9: $Mo/MoSe_2/CZTSe/CdS/PEI/i-ZnO/ITO$ solar cell parameters for different PEI concentrations.

In the best sample, we have practically doubled the cell's efficiency when comparing with the reference, what proves the great potential of this selective contact, even without maximizing the PEI effect as we have buffered it with an intrinsic layer separating the dipoles from the electrode.
Also, if we check the IV curve of these cells, we can see that the shunt and short-circuit troubles seen in previous samples, both in antimony selenide and kesterite absorbers, are here significantly reduced.

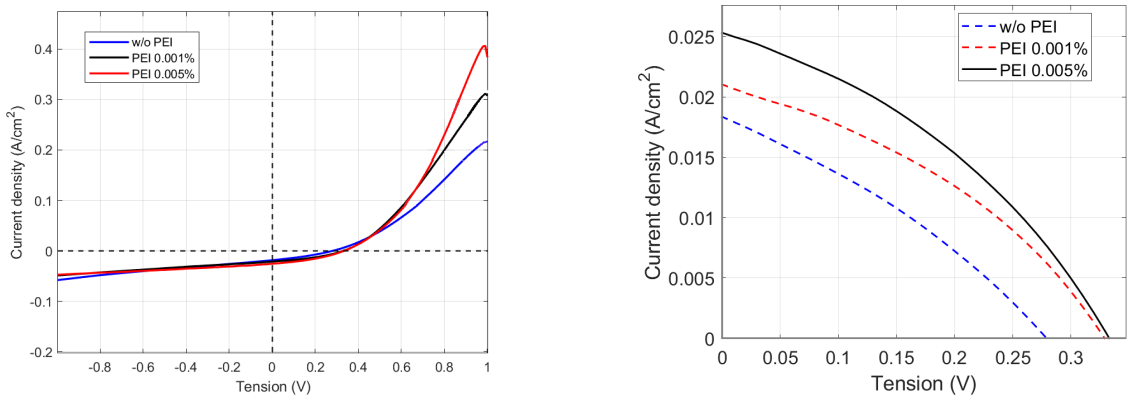

(a) (b)

Figure 3.37: (a) IV curves for $Mo/MoSe_2/CZTSe/CdS/PEI/i-ZnO/ITO$ cells with different PEI concentrations and, (b) amplification of the first quadrant.

In addition, after the depositions, a low temperature annealing treatment is then performed as it has been reported to improve the absorber surface composition and leads to higher efficiencies [91]. This anneling is done using the above-mentioned hotplate and consist on two steps: (1) 25 min under $150°C$ and (2) 10 min at $175°C$, both done in air.

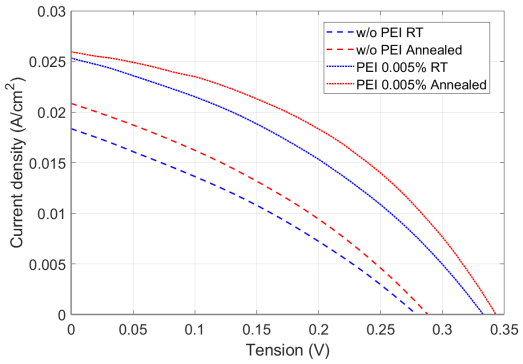

Figure 3.38: Effect of annealing treatment in the cell performance.

	w/o A	With A
$V_{oc}(mV)$	330	340
$J_{sc}(mA/cm^2)$	25.33	25.94
$FF(\%)$	36.69	41.92
$\mu(\%)$	3.066	3.697

Table 3.10: Solar cell parameters comparison before and after the annealing for the highest PEI samples.

As one may notice, the annealing treatment has improved all the cell parameters and in both reference and PEI containing samples, as it is related to an improvement in the absorber and CdS layer. With this final step we have exceed the edge of 40% in the FF for the sample with PEI 0.005%, being the highest value obtained in this study, and a final efficiency close to 4%. Despite of proving the beneficial effect of the PEI layer in this structure, this results are still low when compared with record literature. This could be responsibility of many different factors, but standing out the defects in the absorber and the non-optimal configuration of the window layer, noticeable in the EQE.

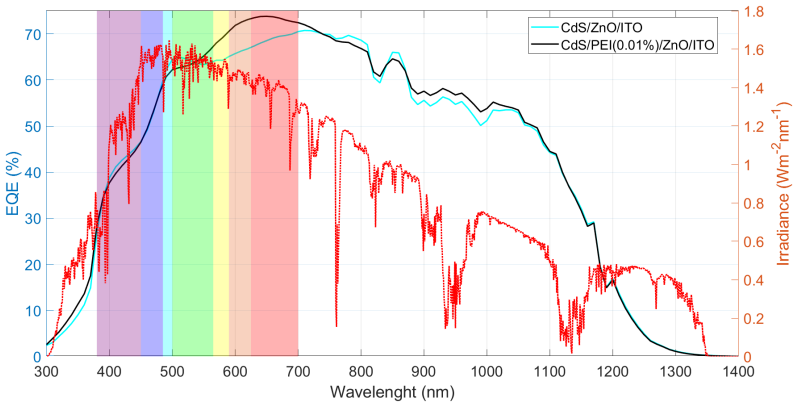

Figure 3.39: External Quantum efficiencies of the CdS kesterite cells with and without PEI.

With this Quantum Efficiency we can see how in long wavelengths an irregular profile is obtained with losses in the EQE at very specific wavelengths. Thus, a problem of wave interference is generated due to the non-optimal thicknesses of the layers conforming the window stack that end to a bad antireflection. Nevertheless with the PEI layer we reach a peak over the 70% of EQE and, also, a higher absorption in the visible range is found. Again, with these measurements one can get the band gap for this kesterite samples: $E_g \approx 1.052eV$

When we try to implement the same window stack to the CdS-free contact checked during the diode tests, TiO_2/PEI, with this titanium dioxide deposited by ALD and having an approximated thickness of 4nm, we obtain a good dark diode but, under light illumination, the photogenerated current is in the wrong quadrant and presents

a "S" shape. This can be attributed to a bad carrier selectivity [92] acting in a similar way as a photoresistance that allow the transport of the majority carriers (holes) across the two contacts. We explain this bad carrier selectivity through two possible reasons. Firstly, the problem could come from the low ETL behaviour of our TiO_2/PEI contact that will require a higher band depletion at the interface, i.e. higher concentrations of PEI or solvents with higher molecular dipole moments. Or, secondly, the fact of using layers of only a couple of nanometers of thickness can bring problems in the uniformality of the coating, specially working with an abosrber whose roughness is of the order of $100nm$. Thus, thicker layer must be employed or the surface roughness has to be reduced, i.e. through $Br_2/MeOH$ chemical etching.

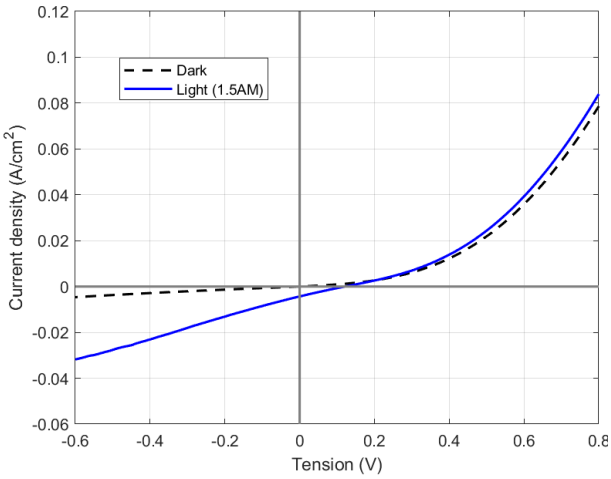

.

Figure 3.40: IV curve for $Mo/MoSe_2/CZTSe/TiO_2(4nm)/PEI(0.001\%)/i-ZnO/ITO$

Chapter 4

Conclusions & Future work

This work has covered a wide range of experiments, starting from PEI contacts characterization over c-Si, passing through the characterization over thin-film absorbers (kesterites and antimony selenide) via diode tests, and ending with their application to different solar cells architectures.
With the TLM characterization, an optimal contact resistivity of 0.236 Ωcm^2 for the PEI interlayer over silicon has been found to be around $1nm$ of thickness, i.e. a concentration of $0.01(wt)\%$ in ethanol. In addition, the "V" shape found when a sweep of thicknesses is done has been attributed (and verified) to the competition between Quantum Tunneling and Thermionic Emission transport mechanisms due to the dipoles present in the PEI layer.
Regarding contact characterization over thin-film absorbers, diode tests have been performed due to the inherent p-type behaviour of these semiconductors. With these experiments, two important conclusions can be extracted. Firstly, the "V" model found in silicon based solar cells is also applicable over kesterites and antimony selenide absorbers. And, secondly, a buffer layer between the absorber and the PEI interlayer is necessary to obtain high-performance devices with low shunts. Moreover, for kesterite devices higher concentrations of PEI appeared to be demanded compared to antimony selenide ones. This is attributed to the great roughness of kesterite surface.
With the results and knowledge acquired throughout the contact characterizations, several solar cells architectures have been tested using these thin-film absrobers and PEI interlayer. With regard to antimony selenide solar cells, a CdS-free stack fully deposited by soft and low-temperature techniques (ALD and spin-coating) involving intrinsic and aluminium-doped zinc oxid and PEI has been proved to show a promising performance. A 2.41% solar cell was obtained and the PEI incorporation has seen to improve the open-circuit voltage of those devices (increases over 40%). This beneficial effect is also observed in kesterite solar cells with standard CdS selective contacts, obtaining a maximum efficiency of 3.697% after an annealing treatment and with a thin PEI interlayer.
Future work could consider studying fractal PEI molecules that would maximize the density of amino groups and, thus, a higher dipole field would be obtained. Furthermore, larger thicknesses of titanium dioxide and PEI in kesterites could be studied to see if electron selectivity is improved and a CdS-free stack is reachable for this absorber. If timid results are obtained even with this study, the i-ZnO stack found for antimony selenide could be transferred to kesterites.

Bibliography

[1] Esteban Ortiz-Ospina Max Roser and Hannah Ritchie. "Life Expectancy". In: *Our World in Data* (2013). https://ourworldindata.org/life-expectancy.

[2] IEA. *Global Energy Review 2019*. 2020. URL: `https://www.iea.org/reports/global-energy-review-2019`.

[3] Monique Hoogwijk and Wina Graus. "Global potential of renewable energy sources: a literature assessment". In: *Background report prepared by order of REN21. Ecofys, PECSNL072975* (2008).

[4] Poul Alberg Østergaard et al. *Sustainable development using renewable energy technology*. 2020.

[5] A. Jager-Waldau. "PV Status Report 2018". In: (2018).

[6] Markus Fischer. "ITRPV 9th edition 2018 report release and key findings". In: *PV CellTech conference*. Vol. 14. 2018.

[7] S Yavuz et al. "Graphene oxide as a p-dopant and an anti-reflection coating layer, in graphene/silicon solar cells". In: *Nanoscale* 8.12 (2016), pp. 6473–6478.

[8] Senlin Diao et al. "12.35% efficient graphene quantum dots/silicon heterojunction solar cells using graphene transparent electrode". In: *Nano Energy* 31 (2017), pp. 359–366.

[9] Dimitri Zielke et al. "Large-area PEDOT: PSS/c-Si heterojunction solar cells with screen-printed metal contacts". In: *Solar RRL* 2.3 (2018), p. 1700191.

[10] Wenbo Ji et al. "Polymeric Electron-Selective Contact for Crystalline Silicon Solar Cells with an Efficiency Exceeding 19%". In: *ACS Energy Letters* 5.3 (2020), pp. 897–902.

[11] Hitoshi Sai et al. "Triple-junction thin-film silicon solar cell fabricated on periodically textured substrate with a stabilized efficiency of 13.6%". In: *Applied Physics Letters* 106.21 (2015), p. 213902.

[12] Priscilla D Antunez et al. "Efficient kesterite solar cells with high open-circuit voltage for applications in powering distributed devices". In: *Nature Energy* 2.11 (2017), pp. 884–890.

[13] Charles Kittel. *Introduction to solid state physics*. 8th ed. New York, NY: John Wiley & Sons, 2005.

[14] Hans Ibach Harald; Lüth. *Solid-state physics: an introduction to principles of materials science*. 4th ed. Berlin: Springer, 2010.

[15] N. David Ashcroft Neil W.; Mermin. *Solid state physics*. 1st ed. Philadelphia: Saunders College, 1976.

[16] Ben G Streetman and Sanjay Banerjee. *Solid state electronic devices*. Prentice-Hall of india, 2001.

[17] Donald A Neamen. *Semiconductor physics and devices: basic principles*. New York, NY: McGraw-Hill, 2012.

[18] Simon Min Sze. *Semiconductor devices: physics and technology*. John wiley & sons, 2008.

[19] David L Pulfrey. "MIS solar cells: A review". In: *IEEE Transactions on Electron Devices* 25.11 (1978), pp. 1308–1317.

[20] SJ Fonash. "Metal-thin film insulator-semiconductor solar cells". In: *11th Photovoltaic Specialists Conference*. 1975, pp. 376–380.

[21] Fatemeh Ansari et al. "Passivation Mechanism Exploiting Surface Dipoles Affords High-Performance Perovskite Solar Cells". In: *Journal of the American Chemical Society* 142.26 (2020), pp. 11428–11433.

[22] Armin G Aber, Stefan Glunz, and Wilhelm Warta. "Field effect passivation of high efficiency silicon solar cells". In: *Solar Energy Materials and Solar Cells* 29.2 (1993), pp. 175–182.

[23] Thomas G Allen et al. "Passivating contacts for crystalline silicon solar cells". In: *Nature Energy* 4.11 (2019), pp. 914–928.

[24] Di Yan et al. "High efficiency n-type silicon solar cells with passivating contacts based on PECVD silicon films doped by phosphorus diffusion". In: *Solar Energy Materials and Solar Cells* 193 (2019), pp. 80–84.

[25] Byungsul Min et al. "A roadmap toward 24% efficient PERC solar cells in industrial mass production". In: *IEEE Journal of Photovoltaics* 7.6 (2017), pp. 1541–1550.

[26] RR King, RA Sinton, and RM Swanson. "Studies of diffused phosphorus emitters: saturation current, surface recombination velocity, and quantum efficiency". In: *IEEE Transactions on electron devices* 37.2 (1990), pp. 365–371.

[27] Vikram V Iyengar, Barada K Nayak, and Mool C Gupta. "Silicon PV devices based on a single step for doping, anti-reflection and surface passivation". In: *Solar Energy Materials and Solar Cells* 94.12 (2010), pp. 2205–2211.

[28] Kazimierz Drabczyk et al. "Comparison of diffused layer prepared using liquid dopant solutions and pastes for solar cell with screen printed electrodes". In: *Microelectronics International* (2016).

[29] Sushobhan Avasthi et al. "Role of majority and minority carrier barriers silicon/organic hybrid heterojunction solar cells". In: *Advanced materials* 23.48 (2011), pp. 5762–5766.

[30] Eloi Ros et al. "Improved Electron Selectivity in Silicon Solar Cells by Cathode Modification with a Dipolar Conjugated Polyelectrolyte Interlayer". In: *ACS Applied Energy Materials* 2.8 (2019), pp. 5954–5959.

[31] Fei Huang, Hongbin Wu, and Yong Cao. "Water/alcohol soluble conjugated polymers as highly efficient electron transporting/injection layer in optoelectronic devices". In: *Chemical Society Reviews* 39.7 (2010), pp. 2500–2521.

[32] Dimitri Zielke et al. "Organic-silicon solar cells exceeding 20% efficiency". In: *Energy Procedia* 77 (2015), pp. 331–339.

[33] Luis G Gerling et al. "Transition metal oxides as hole-selective contacts in silicon heterojunctions solar cells". In: *Solar Energy Materials and Solar Cells* 145 (2016), pp. 109–115.

[34] Corsin Battaglia et al. “Silicon heterojunction solar cell with passivated hole selective MoOx contact”. In: *Applied Physics Letters* 104.11 (2014), p. 113902.

[35] Gerard Masmitjà et al. “V2Ox-based hole-selective contacts for c-Si interdigitated back-contacted solar cells”. In: *Journal of materials chemistry A* 5.19 (2017), pp. 9182–9189.

[36] Junfeng Wei et al. “Roll-to-roll printed stable and thickness-independent ZnO: PEI composite electron transport layer for inverted organic solar cells”. In: *Solar Energy* 193 (2019), pp. 102–110.

[37] Kang Min Kim et al. “Work function optimization of vacuum free top-electrode by PEDOT: PSS/PEI interaction for efficient semi-transparent perovskite solar cells”. In: *Solar Energy Materials and Solar Cells* 176 (2018), pp. 435–440.

[38] Matthew T Fontana et al. “Evaporation vs Solution Sequential Doping of Conjugated Polymers: F4TCNQ Doping of Micrometer-Thick P3HT Films for Thermoelectrics”. In: *The Journal of Physical Chemistry C* 123.37 (2019), pp. 22711–22724.

[39] K Li et al. “Novel wood adhesives from condensed tannins and polyethylenimine”. In: *International journal of adhesion and adhesives* 24.4 (2004), pp. 327–333.

[40] Anke von Harpe et al. “Characterization of commercially available and synthesized polyethylenimines for gene delivery”. In: *Journal of Controlled Release* 69.2 (2000), pp. 309–322.

[41] Omprakash Yemul and Toyoko Imae. “Synthesis and characterization of poly (ethyleneimine) dendrimers”. In: *Colloid and Polymer Science* 286.6 (2008), pp. 747–752.

[42] Lourdes Pastor-Pérez et al. “Unprecedented blue intrinsic photoluminescence from hyperbranched and linear polyethylenimines: polymer architectures and pH-effects”. In: *Macromolecular rapid communications* 28.13 (2007), pp. 1404–1409.

[43] Martin A Green. “Radiative efficiency of state-of-the-art photovoltaic cells”. In: *Progress in Photovoltaics: Research and Applications* 20.4 (2012), pp. 472–476.

[44] Dávid Strachala et al. “Methods for recycling photovoltaic modules and their impact on environment and raw material extraction.” In: *Acta Montanistica Slovaca* 22.3 (2017).

[45] D Bernhardt and IIJF Reilly. “Mineral commodity summaries 2020”. In: *US Geological Survey* (2020).

[46] Arnulf Jäger-Waldau. “Snapshot of photovoltaics—February 2019”. In: *Energies* 12.5 (2019), p. 769.

[47] P Jayarama Reddy. *Solar power generation: technology, new concepts & policy*. CRC Press, 2012.

[48] KL Chopra, PD Paulson, and V Dutta. “Thin-film solar cells: an overview”. In: *Progress in Photovoltaics: Research and applications* 12.2-3 (2004), pp. 69–92.

[49] Taesoo D Lee and Abasifreke U Ebong. “A review of thin film solar cell technologies and challenges”. In: *Renewable and Sustainable Energy Reviews* 70 (2017), pp. 1286–1297.

[50] Martin A Green. “Thin-film solar cells: review of materials, technologies and commercial status”. In: *Journal of Materials Science: Materials in Electronics* 18.1 (2007), pp. 15–19.

[51] Jonathan Gifford. “Solar Frontier hits 22.3% on CIGS cell”. In: *pv magazine* (2015).

[52] Russell M Geisthardt, Marko Topič, and James R Sites. "Status and potential of CdTe solar-cell efficiency". In: *IEEE Journal of photovoltaics* 5.4 (2015), pp. 1217–1221.

[53] Hironori Katagiri et al. "Preparation and evaluation of Cu2ZnSnS4 thin films by sulfurization of E B evaporated precursors". In: *Solar Energy Materials and Solar Cells* 49.1-4 (1997), pp. 407–414.

[54] LL Kazmerski et al. "Growth and characterization of thin-film compound semiconductor photovoltaic heterojunctions". In: *Journal of Vacuum Science and Technology* 14.1 (1977), pp. 65–68.

[55] Teoman Taskesen et al. "Resilient and reproducible processing for CZTSe solar cells in the range of 10%". In: *Progress in Photovoltaics: Research and Applications* 26.12 (2018), pp. 1003–1006.

[56] Minlin Jiang and Xingzhong Yan. "Cu2ZnSnS4 thin film solar cells: present status and future prospects". In: *Solar Cells—Research and Application Perspectives* (2013).

[57] Sergio Giraldo et al. "Progress and perspectives of thin film kesterite photovoltaic technology: a critical review". In: *Advanced materials* 31.16 (2019), p. 1806692.

[58] DS Albin et al. "The effect of copper vacancies on the optical bowing of chalcopyrite Cu (In, Ga) Se 2 alloys". In: *MRS Online Proceedings Library Archive* 228 (1991).

[59] S Giraldo et al. "How small amounts of Ge modify the formation pathways and crystallization of kesterites". In: *Energy & Environmental Science* 11.3 (2018), pp. 582–593.

[60] Simon López-Marino et al. "The importance of back contact modification in Cu2ZnSnSe4 solar cells: the role of a thin MoO2 layer". In: *Nano Energy* 26 (2016), pp. 708–721.

[61] Xinchen Li et al. "Achieving 11.95% efficient Cu 2 ZnSnSe 4 solar cells fabricated by sputtering a Cu–Zn–Sn–Se quaternary compound target with a selenization process". In: *Journal of Materials Chemistry A* 7.16 (2019), pp. 9948–9957.

[62] Markus Neuschitzer et al. "Optimization of CdS buffer layer for high-performance Cu2ZnSnSe4 solar cells and the effects of light soaking: elimination of crossover and red kink". In: *Progress in Photovoltaics: Research and Applications* 23.11 (2015), pp. 1660–1667.

[63] John Emsley. *Nature's building blocks: an AZ guide to the elements*. Oxford University Press, 2011.

[64] Rokas Kondrotas, Chao Chen, and Jiang Tang. "Sb2S3 solar cells". In: *Joule* 2.5 (2018), pp. 857–878.

[65] CD Lokhande. "Chemical deposition of metal chalcogenide thin films". In: *Materials Chemistry and Physics* 27.1 (1991), pp. 1–43.

[66] Jianwang Zhang et al. "All antimony chalcogenide tandem solar cell". In: *Solar RRL* 4.4 (2020), p. 2000048.

[67] Yu Cao et al. "Theoretical Insight into High-Efficiency Triple-Junction Tandem Solar Cells via the Band Engineering of Antimony Chalcogenides". In: *Solar RRL* 5.4 (2021), p. 2000800.

[68] Xiaomin Wang et al. "Development of antimony sulfide–selenide Sb2 (S, Se) 3-based solar cells". In: *Journal of energy chemistry* 27.3 (2018), pp. 713–721.

[69] Yong Chan Choi et al. “Sb2Se3-sensitized inorganic–organic heterojunction solar cells fabricated using a single-source precursor”. In: *Angewandte Chemie* 126.5 (2014), pp. 1353–1357.

[70] Xixing Wen et al. “Magnetron sputtered ZnO buffer layer for Sb2Se3 thin film solar cells”. In: *Solar Energy Materials and Solar Cells* 172 (2017), pp. 74–81.

[71] Hui Deng et al. “Efficient and stable TiO2/Sb2S3 planar solar cells from absorber crystallization and Se-atmosphere annealing”. In: *Materials Today Energy* 3 (2017), pp. 15–23.

[72] Ghenadii Korotcenkov. *Metal Oxide Powder Technologies: Fundamentals, Processing Methods and Applications*. Elsevier, 2020.

[73] Olayinka Oluwatosin Abegunde et al. “Overview of thin film deposition techniques”. In: *AIMS Materials Science* 6.2 (2019), pp. 174–199.

[74] Markku Leskelä and Mikko Ritala. “Atomic layer deposition (ALD): from precursors to thin film structures”. In: *Thin solid films* 409.1 (2002), pp. 138–146.

[75] Nam-Trung Nguyen. “Chapter 4 - Fabrication technologies”. In: *Micromixers (Second Edition)*. Ed. by Nam-Trung Nguyen. Second Edition. Micro and Nano Technologies. Oxford: William Andrew Publishing, 2012, pp. 113–161. ISBN: 978-1-4377-3520-8.

[76] Richard Smith, Hiroshi Inomata, and Cor Peters. “Chapter 4 - Historical Background and Applications”. In: *Introduction to Supercritical Fluids*. Ed. by Richard Smith, Hiroshi Inomata, and Cor Peters. Vol. 4. Supercritical Fluid Science and Technology. Elsevier, 2013, pp. 175–273.

[77] Sidhant Grover. “Effect of transmission line measurement (TLM) geometry on specific contact resistivity determination”. In: (2016).

[78] C. J. Coelho Santana. “Sofware de control de un trazador de características en Matlab para la caracterización de células solares”. FDP dissertation. UPC, Escola Tècnica Superior d’Enginyeria de Telecomunicacio de Barcelona, 2015.

[79] CA Mead. *Physics of interfaces*. Electrochem. Soc. New York, NY: B. Schwartz, 1969.

[80] Iman Gharibshahian, Ali A Orouji, and Samaneh Sharbati. “Alternative buffer layers in Sb2Se3 thin-film solar cells to reduce open-circuit voltage offset”. In: *Solar Energy* 202 (2020), pp. 294–303.

[81] Liang Wang et al. “Stable 6%-efficient Sb 2 Se 3 solar cells with a ZnO buffer layer”. In: *Nature Energy* 2.4 (2017), pp. 1–9.

[82] Vedentam Srikant and David R Clarke. “On the optical band gap of zinc oxide”. In: *Journal of Applied Physics* 83.10 (1998), pp. 5447–5451.

[83] K Jacobi, G Zwicker, and A Gutmann. “Work function, electron affinity and band bending of zinc oxide surfaces”. In: *Surface Science* 141.1 (1984), pp. 109–125.

[84] SH Jeong and JH Boo. “Influence of target-to-substrate distance on the properties of AZO films grown by RF magnetron sputtering”. In: *Thin Solid Films* 447 (2004), pp. 105–110.

[85] G Masmitjà et al. “Interdigitated back-contacted crystalline silicon solar cells with low-temperature dopant-free selective contacts”. In: *Journal of Materials Chemistry A* 6.9 (2018), pp. 3977–3985.

[86] M Atowar Rahman. "Enhancing the photovoltaic performance of Cd-free Cu2ZnSnS4 heterojunction solar cells using SnS HTL and TiO2 ETL". In: *Solar Energy* 215 (2021), pp. 64–76.

[87] JH Shi et al. "Effect of ZnO buffer layer on AZO film properties and photovoltaic applications". In: *Journal of Materials Science: Materials in Electronics* 21.10 (2010), pp. 1005–1013.

[88] Dagang Miao et al. "Highly transparent and infrared reflective AZO/Ag/AZO multilayer film prepared on PET substrate by RF magnetron sputtering". In: *Vacuum* 106 (2014), pp. 1–4.

[89] Do-Joong Lee et al. "Structural and electrical properties of atomic layer deposited Al-doped ZnO films". In: *Advanced Functional Materials* 21.3 (2011), pp. 448–455.

[90] Oliver S Hutter et al. "6.6% efficient antimony selenide solar cells using grain structure control and an organic contact layer". In: *Solar Energy Materials and Solar Cells* 188 (2018), pp. 177–181.

[91] Markus Neuschitzer et al. "Complex surface chemistry of kesterites: Cu/Zn reordering after low temperature postdeposition annealing and its role in high performance devices". In: *Chemistry of Materials* 27.15 (2015), pp. 5279–5287.

[92] Christoph Messmer et al. "Numerical simulation of silicon heterojunction solar cells featuring metal oxides as carrier-selective contacts". In: *IEEE Journal of Photovoltaics* 8.2 (2018), pp. 456–464.